Statistical Analysis of Discrete Aurora on Mars: Variability with Magnetic Topology, Local Time and Season

Krishnaprasad Chirakkil[1,2,3], Robert J. Lillis[3], Justin Deighan[1], Michael S. Chaffin[1], Sonal K. Jain[1], David A. Brain[1], Matthew O. Fillingim[3], Raghuram Susarla[1,2], Greg Holsclaw[1], Xiaohua Fang[1], Nick M. Schneider[1], Hoor AlMazmi[4], Hessa AlMatroushi[5], Marko Gacesa[2,6], Nayla El-Kork[2,6]

[1]Laboratory for Atmospheric and Space Physics, University of Colorado Boulder, Boulder, CO, USA
[2]Space and Planetary Science Center, Khalifa University, Abu Dhabi, UAE
[3]Space Sciences Laboratory, University of California, Berkeley, CA, USA
[4]United Arab Emirates Space Agency, Abu Dhabi, UAE
[5]Mohammed Bin Rashid Space Centre, Dubai, UAE
[6]Department of Physics, Khalifa University, Abu Dhabi, UAE

Key Points:

- Higher aurora occurrence is observed in regions with open magnetic topology and vertical crustal fields
- More aurora occurs near–terminator compared to midnight, with higher occurrence at dusk than dawn
- Aurora shows seasonal dependence that follows the seasonal variability in ionospheric photoelectrons

February 14, 2024

Corresponding author: Krishnaprasad Chirakkil, krishnaprasad.chirakkil@lasp.colorado.edu, kpchirakkil@gmail.com

Abstract

We present a comprehensive study of the nightside discrete electron aurora phenomenon on Mars, utilizing observations from the Emirates Mars Ultraviolet Spectrometer (EMUS) onboard the Emirates Mars Mission (EMM). The oxygen emission at 130.4 nm is by far the brightest FUV (far ultraviolet) auroral emission line observed at Mars. We identify auroral pixels in OI 130.4 nm disk observations, with higher sensitivity than previously possible. Our statistical analysis reveals regional, solar zenith angle, local time, and seasonal dependencies of auroral occurrence. Higher occurrence of aurora is observed in regions of open magnetic topology and vertical crustal magnetic fields. Aurora occurs more frequently closer to the terminator and is more likely on the dusk versus dawn sides of the night hemisphere. A pronounced auroral feature appears close to midnight local times in the southern hemisphere, consistent with the "spot" of energetic electron fluxes previously identified in the Mars Global Surveyor (MGS) data. The auroral spot is more frequent after midnight than before. Additionally, some regions on Mars are "aurora voids" where essentially no aurora occurs. The non–crustal field aurora exhibits a seasonal dependence, with major enhancements around L_S 235° (near perihelion) and L_S 30°. This is in line with the seasonal variability in ionospheric Total Electron Content (TEC) observed by Mars Express, which is in turn related to the variability of solar irradiance and thermospheric density. Aurora occurrence also shows an increase with the rise of Solar Cycle 25. These observations not only shed light on where and when Martian aurora occurs, but also add to our understanding of Mars' magnetic environment and its interaction with the heliospheric environment.

Plain Language Summary

In our study, we explore the fascinating phenomenon of aurora on the nightside of Mars, using observations from the highly sensitive Emirates Mars Ultraviolet Spectrometer on the Emirates Mars Mission. Our analysis reveals distinct patterns in aurora occurrence on the planet. For instance, there's a higher rate of auroral activity in regions where Mars' magnetic field lines are open to space and in places with strong vertical magnetic fields. We also found that aurora is more common near the terminator, and particularly during the evening hours, as opposed to early morning. Interestingly, these Martian light shows also have a seasonal rhythm, peaking around specific times in a Martian year. This seasonal pattern aligns with the seasonal variation of photoelectrons in Mars' ionosphere. Our study not only gives us a clearer picture of where and when the aurora occurs on Mars but also hints at the underlying processes influencing them, offering insights into the planet's magnetic and charged particle environment.

1 Nightside Discrete Electron Aurora on Mars

Mars discrete electron aurora, first identified by the SPICAM (SPectroscopy for the Investigation of the Characteristics of the Atmosphere of Mars) ultraviolet spectrometer on Mars Express (Bertaux et al., 2005; Bertaux et al., 2006; Leblanc et al., 2006; Soret et al., 2016), are spatially confined photon emissions in Mars' nightside upper atmosphere, generated by the decay of electronic states in atoms and molecules excited by suprathermal electrons (> a few eV). These discrete aurorae (a total of 19 detections by SPICAM: 16 in nadir mode and 3 in limb mode), distinguishable by their small spatial scales and association with strong vertical crustal magnetic fields, differ significantly from other Mars auroral types (Haider et al., 2022): diffuse aurora, caused by the global precipitation of solar energetic particles (Schneider et al., 2015; Gérard et al., 2017; Nakamura et al., 2022; Schneider et al., 2018), and proton aurora, resulting from solar wind protons directly entering the upper atmosphere after charge exchange with neutral hydrogen in the corona (Deighan et al., 2018; Hughes et al., 2019; Ritter et al., 2018; Gérard et al., 2019; Chaffin et al., 2022).

The Mars Atmosphere and Volatile EvolutioN (MAVEN) Imaging Ultraviolet Spectrograph (IUVS) has expanded our understanding with over 400 detections of discrete aurora (278 detections in limb mode and 126 detections in nadir mode), revealing different behaviors within and outside Mars' strong crustal magnetic field region or "mini–magnetosphere" in the southern hemisphere which is near 177°E and 52°S (Schneider et al., 2021; Girazian et al., 2022; Johnston et al., 2023; Bowers et al., 2023; Soret et al., 2021; Fang et al., 2022). Both MEX (Mars Express) and MAVEN observations of discrete aurorae are mainly focused on mid ultraviolet (MUV) emissions, such as CO Cameron bands (190 to 270 nm), CO_2^+ UV doublet (at 288–289 nm), and the oxygen forbidden emission (at 297.2 nm) due to their higher brightness (Gérard et al., 2015; Schneider et al., 2018; Soret et al., 2021).

The Emirates Mars Ultraviolet Spectrograph (EMUS) on the Emirates Mars Mission (EMM) spacecraft (Amiri et al., 2022) has further advanced this research. With its large orbit and greater sensitivity in the extreme and far ultraviolet range ($\sim$ 85 – 180 nm), EMM/EMUS has enabled systematic synoptic (disk) nearly global observations of Mars' upper atmosphere (Holsclaw et al., 2021). Using EMUS observations, Chaffin et al. (2022) reported patchy proton aurora emissions in the dayside Martian atmosphere at hydrogen Lyman alpha and Lyman beta wavelengths. Furthermore, England et al. (2022) reported dayglow structures in the EMUS observations of several disk emissions including OI 130.4 nm.

Lillis et al. (2022) presented the first synoptic images of nightside discrete aurora using EMUS observations, detecting discrete aurora in over 75% of images during a time of mostly low solar activity. The oxygen emission lines (at 130.4 nm and 135.6 nm among others), carbon monoxide (CO) emission lines including the Fourth Positive Group (CO 4PG) band emission, and carbon emission lines are prominent among the detected extreme/far ultraviolet (EUV/FUV) auroral emission features. This is expected for electron impact on CO_2, O, and CO resulting in a range of excited states of O and CO. Lillis et al. (2022) classified the discrete auroral features captured by EMUS as crustal field aurora in regions of strong crustal magnetic fields (e.g., Figure 1a), non–crustal field sinuous aurora which are elongated, filamentary emissions usually formed away from strong crustal fields (e.g., Figure 1b), and non–crustal field patchy aurora in spatially extended weak crustal field regions often with less defined edges (e.g., Figure 1c). Note that all three types of discrete aurora can appear simultaneously at different locations on the nightside (Lillis et al., 2022; Atri et al., 2022; Pacios et al., 2024). However, these studies used limited data sets and did not provide in–depth analyses of Mars' discrete aurora, its variability, and drivers.

We use OI 130.4 nm triplet emission (result of an electric dipole allowed resonance transition $^3S \rightarrow {}^3P$ of atomic oxygen), which is brightest FUV auroral emission feature in the Martian atmosphere – with the highest signal–to–noise ratio – for the analysis presented in this study. The following sections describe the instrument and data used, dependence of aurora on crustal field, magnetic topology, solar zenith angle (SZA), local time, and season. Finally, the paper concludes by summarizing the analysis and describing the prospects for future work.

2 EMM EMUS Disk Observations

The Emirates Mars Mission (EMM) spacecraft, orbiting every approximately 55 hours in a $\sim$ 20,000 $\times$ 43,000 km altitude (6.9 $\times$ 13.7 Mars radii) science orbit inclined at 25°, provides near–complete geographic and diurnal coverage of Mars every approximately 10 days (Amiri et al., 2022; Almatroushi et al., 2021). Emirates Mars Ultraviolet Spectrometer (EMUS), an EUV/FUV spectrometer mounted on the instrument deck of the EMM orbiter, records photon counts from $\sim$ 85 – 180 nm UV light in each pixel. The light enters through a narrow 0.6° x 11° aperture (or "slit") and is directed by a spherical mirror onto a diffraction grating, which then splits the light into its spectral components. This process results in a two–dimensional image (one spatial and one spectral dimension) on the detector, which

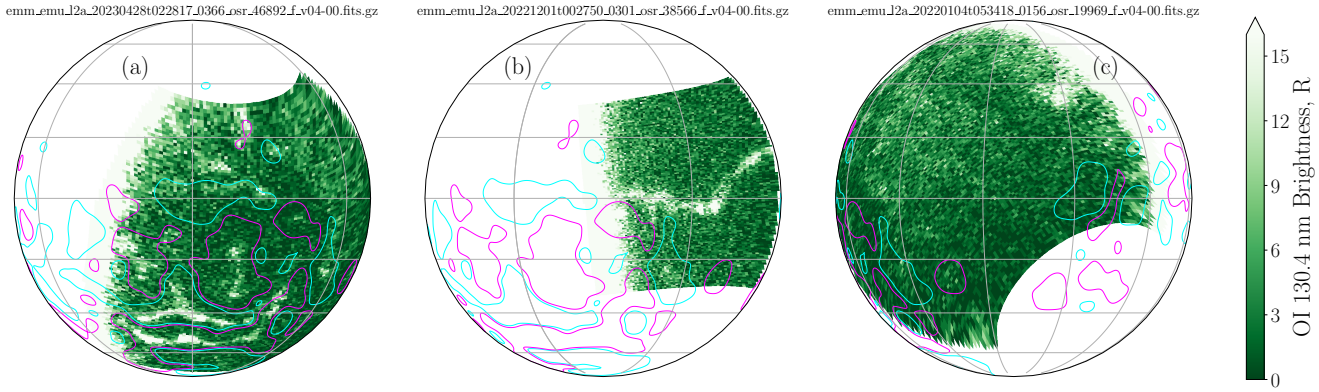

Figure 1. EMUS disk images of OI 130.4 nm emission showing examples of crustal field aurora and non–crustal field aurora: a) crustal field aurora on 2023/04/28, b) sinuous non–crustal field aurora on 2022/12/01, and c) patchy non–crustal field aurora on 2022/01/04. The cyan and magenta contours are radial (i.e., vertical) component of crustal magnetic field at -10 nT and 10 nT respectively at an altitude of 400 km based on the model of Langlais et al. (2019).

consists of a microchannel plate stack with a cesium iodide photocathode and a photon–counting, cross-delay line anode that enables spectral–spatial imaging (Holsclaw et al., 2021).

EMUS operates in various observation strategies (OS), including OS1, OS2, and OSr, where the slit field–of–view is dragged slowly (about 13–21 minutes) across the disk of Mars as seen from the spacecraft (with 7.1, 6, and 10.7 seconds integrations for OS1, OS2, and OSr respectively). OSr involves a single swath covering most of the disk, OS1 consists of two overlapping swaths, and OS2 comprises two or three swaths depending on EMM's distance from Mars, covering the disk and inner corona (Holsclaw et al., 2021). This allows for the reconstruction of images at any desired wavelength for each swath. Holsclaw et al. (2021) provides a detailed description of the EMUS instrument, its data collection modes, and science goals.

This study has examined the EMUS disk dataset acquired between 2021-04-21 and 2023-08-31, which is a total of 4879 swaths (or individual images) scanning both dayside and nightside combining OS1 (454 swaths), OS2 (1979 swaths) and OSr (2446 swaths). We restricted the solar zenith angle (SZA) and phase angle to be greater than 120°, ensuring sufficient nightside disk coverage, with emission angle less than 88°, to observe discrete aurora if present. The SZA criterion is for picking the nightside pixels that are not contaminated by the UV dayglow (primarily produced by resonant scattering of sunlight at UV) and are away from the UV terminator (Lillis et al., 2022). The phase angle criterion is introduced to remove any dayside oxygen exosphere foreground contribution to the auroral brightness. The emission angle criterion is set to get just the disk pixels and to avoid any inner corona pixels. The altitude of the discrete aurora emission is around ∼130 km near the ionospheric peak (Soret et al., 2021). These criteria reduced our dataset to 1319 swaths (consisting of 732, 538, and 49 swaths in OSr, OS2, and OS1 respectively), comprising a total of $\sim 6.08 \times 10^6$ pixels on the nightside. We also removed any hydrogen Lyman alpha background to OI 130.4 nm emission by subtracting the H Lyman alpha wing from 130.4 nm oxygen emission (Chirakkil et al., 2023).

Figure 1 shows three examples of EMUS disk swath observations on the nightside (in orthographic projection) with discrete aurora in OI 130.4 nm emission. Figure 1a is a crustal field aurora, where the auroral emission is from a strong crustal field region in the southern hemisphere ("the mini–magnetosphere"), Figures 1b and 1c are examples of non–crustal

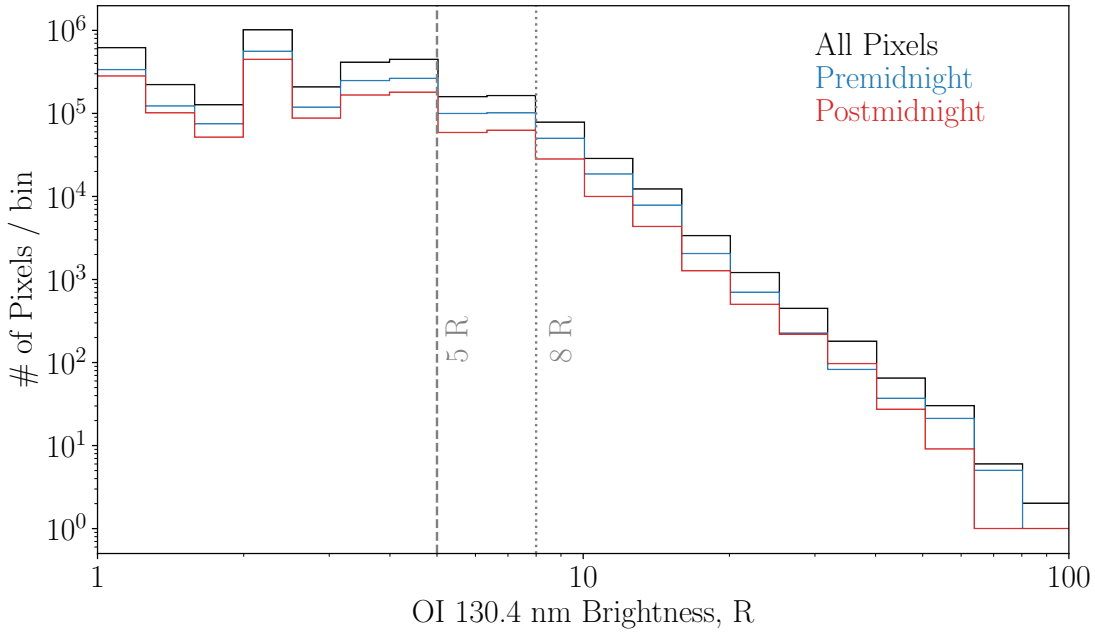

Figure 2. Histograms showing the number of pixels in logarithmic brightness bins for all nightside pixels (in black), divided into pre–midnight pixels (in blue), and post–midnight pixels (in red). Vertical gray lines show the brightness thresholds of 5 R (dashed line) and 8 R (dotted line).

field sinuous aurora and non–crustal field patchy aurora respectively, where the emission is from regions away from the strong crustal fields. The contours of radial crustal field at -10 nT (cyan) and 10 nT (magenta) are also shown for context (Langlais et al., 2019; Lillis et al., 2022). We can notice that the non–crustal field aurora (both patchy and sinuous) are connected to the dayside terminator, and this is commonly observed.

3 Crustal Field and Magnetic Topology Dependence of Aurora

Figure 2 shows the brightness histograms of all the nightside pixels, as well as the histograms divided into pre–midnight pixels (before 12 am) and post–midnight pixels (after 12 am). An aurora is detected using a fixed brightness threshold following Lillis et al. (2022). The OI 130.4 nm emission brightness thresholds of 5 R and 8 R are also shown in Figure 2. At all brightness levels, the pre–midnight pixel counts are higher than the post–midnight pixel counts.

Figure 3 shows the occurrence of aurora in geographic latitude and longitude. Occurrence is calculated as a fraction of aurora pixels to all nightside pixels in each bin. Here we used 1° by 1° geographic bins. We did a pixel subsampling (by dividing each individual pixel into four subpixels) for better statistics and improved spatial resolution. A Gaussian filter is applied in the geographic maps to reduce the noise. The upper and lower panels depict the geographic occurrence maps for 5 R and 8 R thresholds, respectively, in OI 130.4 nm emission. The crustal field contours of -10 nT (green) and 10 nT (blue) are also shown. We can see that the strong crustal field regions display a higher aurora occurrence that is localized and discrete, especially in the southern hemisphere and near the equator. The aurora occurrence is reduced for a threshold of 8 R as compared to 5 R. This aligns with the trend in Figure 2, where the number of auroral pixels decreases with increasing auroral brightness.

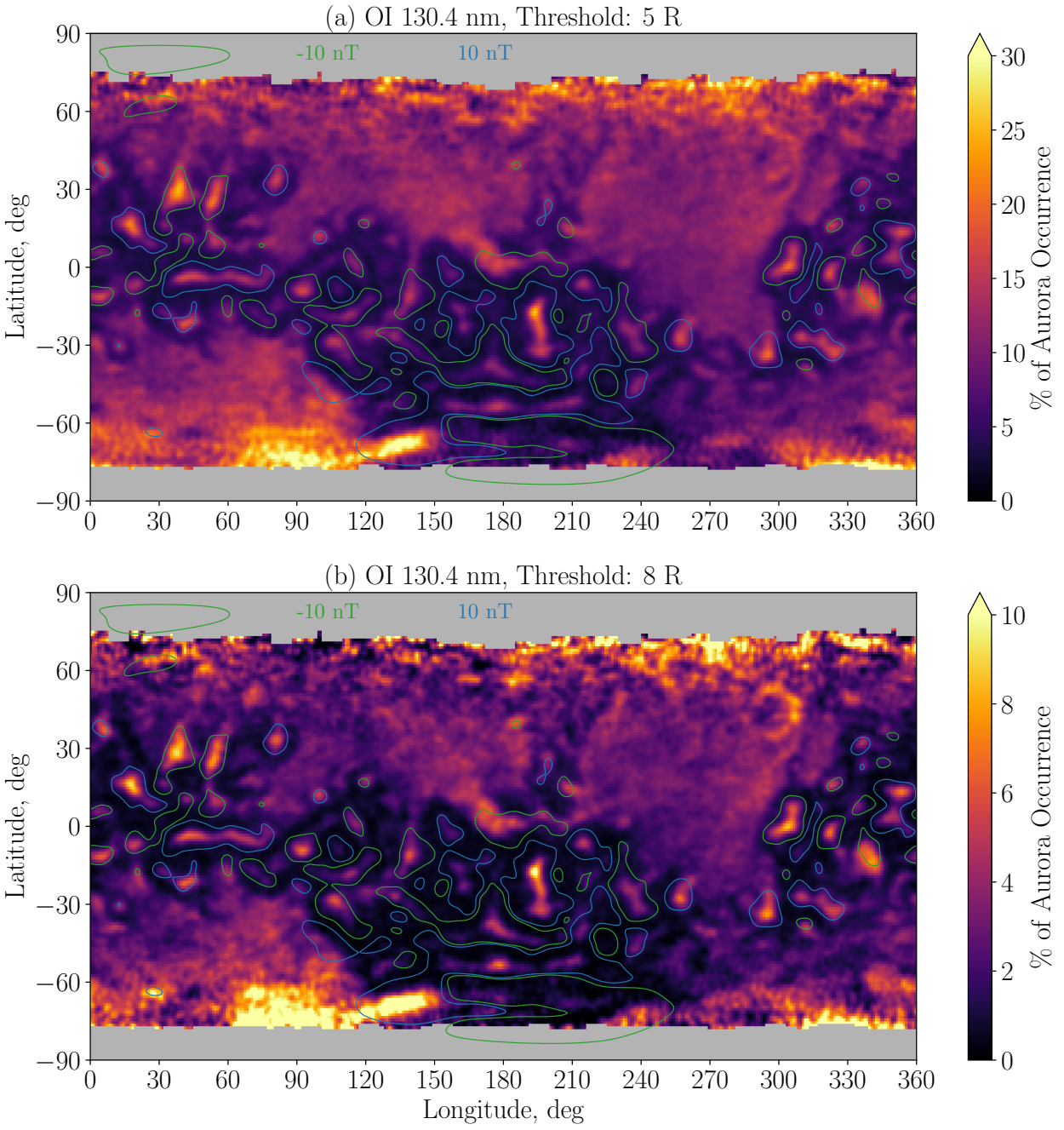

Figure 3. Geographic occurrence of discrete aurora in OI 130.4 nm emission using brightness thresholds of a) 5 R and b) 8 R. Green and blue contours are the -10 nT and 10 nT levels of radial component of crustal magnetic field respectively, at 400 km altitude according the model of Langlais et al. (2019).

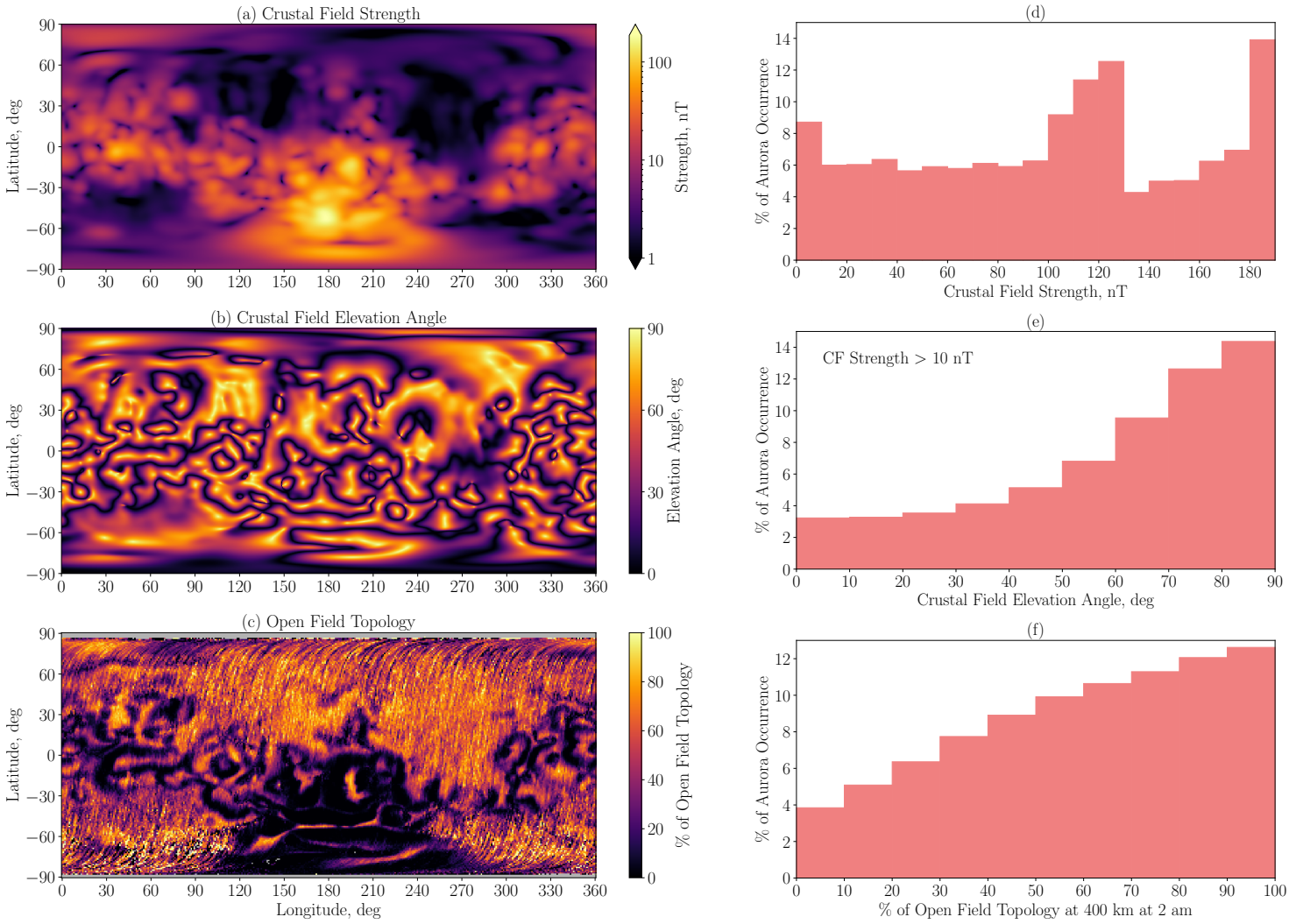

Figure 4. Geographic maps showing Mars' a) crustal magnetic field strength ($B = \sqrt{B_r^2 + B_t^2 + B_p^2}$), b) crustal magnetic field elevation angle (Elevation Angle = $\arctan\left(\frac{|B_r|}{\sqrt{B_t^2+B_p^2}}\right)$), both at 400 km altitude according to the model of Langlais et al. (2019), and c) open field topology probability at 400 km altitude at 2 am local time from Brain et al. (2007). Histograms showing aurora occurrence d) as a function of crustal field strength, e) as a function of crustal field elevation angle (for crustal field strength greater than 10 nT), and f) as a function of probability of open field topology.

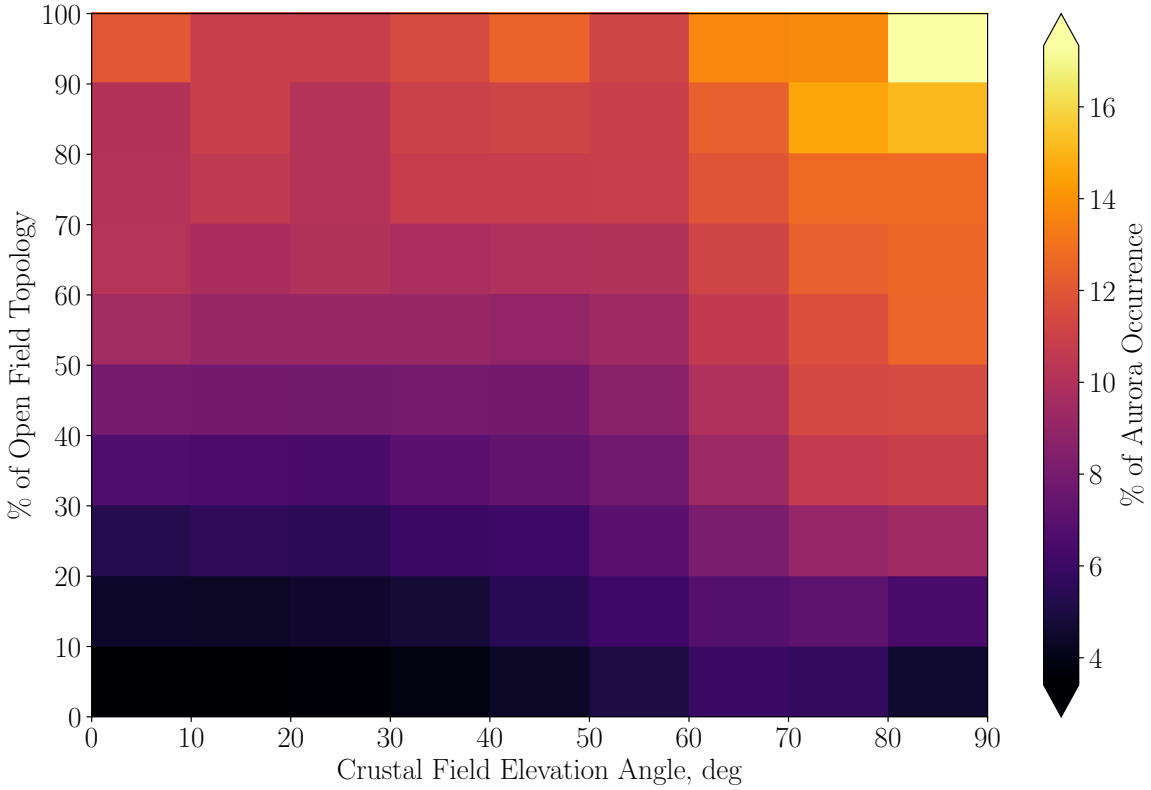

Figure 5. Aurora occurrence as a function of crustal field elevation angle at 400 km (Langlais et al., 2019) and probability of open field topology at 400 km at 2 am (Brain et al., 2007). Aurora occurrence is highest for the bin of 90–100% open field topology and 80–90° crustal field elevation angle.

In addition to the bright crustal field patches, we also notice large areas of "aurora voids", where the aurora occurrence is nearly zero. This is analogous to "plasma voids" observed by Mars Global Surveyor (MGS) spacecraft, and are seemed to be observed where closed crustal magnetic loops existed at 400 km on the nightside – i.e., they did not connect with the magnetosphere, and hence, suprathermal electrons could not access them (Mitchell et al., 2001; Steckiewicz et al., 2017; Brain et al., 2007; Lillis & Brain, 2013). A strong auroral occurrence feature in the southern hemisphere between $\sim$ 60 to 150 degrees east longitude and $\sim$ 60°S to 75°S latitude is consistent with the "spot" of energetic electron fluxes identified in MGS data at 2 am (Brain et al., 2007), which has also been numerically predicted by Fang et al. (2022). Additionally, we can see significant aurora occurrence in regions away from these strong crustal fields. These are more diffuse features (i.e., with less clear edges) in the occurrence map and are the result of mostly non–crustal field patchy aurora, but also less–common sinuous aurora. The coverage at high latitudes (near the poles) is poor due to the SZA cut–off at 120°. The geographic maps with both 5 R and 8 R thresholds are similar, except that the features become more sharp (with distinct boundaries) at higher brightness threshold. Hence for the rest of the analysis, we use a brightness threshold of 5 R for better pixel statistics, due to the greater number of pixels falling above that threshold and O corona background emission of the nightside almost never exceeding 5 R (Lillis et al., 2022).

Now that we know there is a crustal field dependence for discrete aurora, let us examine it in detail. Figure 4(a–c) shows the geographic maps of crustal field strength (Figure 4a), crustal field elevation angle (Figure 4b), and probability of open field topology (Figure 4c). The crustal field data at 400 km altitude is according to the model of Langlais et al. (2019), which combines MGS magnetometer, MGS Electron Reflectometer, and MAVEN magnetometer data. The open field topology data is from Brain et al. (2007). The magnetic topology map shows the probability of open field lines at 400 km altitude as estimated through electron pitch angle distributions from MGS Magnetometer and Electron Reflectometer (MAG/ER). One–sided loss cones are indicative of open field topology, while two–sided loss cones are indicative of closed field topology. The measurements were made at 400 km altitude around 2 am local time on the nightside due to the near circular and Sun–synchronous orbit of the MGS spacecraft (Brain et al., 2007).

Figure 4(d–f) shows the histograms of aurora occurrence as a function of crustal field strength (Figure 4d), crustal field elevation angle (Figure 4e), and open field topology (Figure 4f). Here also, the occurrence is calculated as fraction of aurora pixels to the total pixels in each bin. Only the elevation angles for CF strength more than 10 nT are used. These are global occurrence rates averaged over all geographic locations. We can see that the aurora occurrence increases with both higher open field topology as well as higher elevation angles (i.e., vertical crustal fields), while the aurora occurrence is not directly proportional to CF strength. This is due to the fact that there is a higher geographic occurrence in regions away from the strong crustal fields due to non–crustal field aurorae. As mentioned previously, both MEX/SPICAM and MAVEN/IUVS observations were largely focused on the crustal field aurora and thus obtained a direct correlation with CF strength (Gérard et al., 2015; Schneider et al., 2021).

Figure 5 shows the aurora occurrence as a function of crustal field elevation angle and probability of open field topology. Occurrence is calculated as fraction of aurora pixels to the total nightside pixels in each bin. Aurora occurrence is highest for the bin of 90–100% open field topology and 80–90° crustal field elevation angle. Also, in general, higher aurora occurrence is observed when the probability of open field topology is larger than 50% and crustal field elevation angle greater than 60°. However, when the probability of open field topology is less than 20%, the aurora occurrence is lower, even for larger crustal field elevation angles. Similarly, when the probability of open field topology is larger than 50%, aurora occurrence is higher, even when the crustal field elevation angle is smaller. In this context, it is important to note that at 400 km altitude, the induced magnetic field

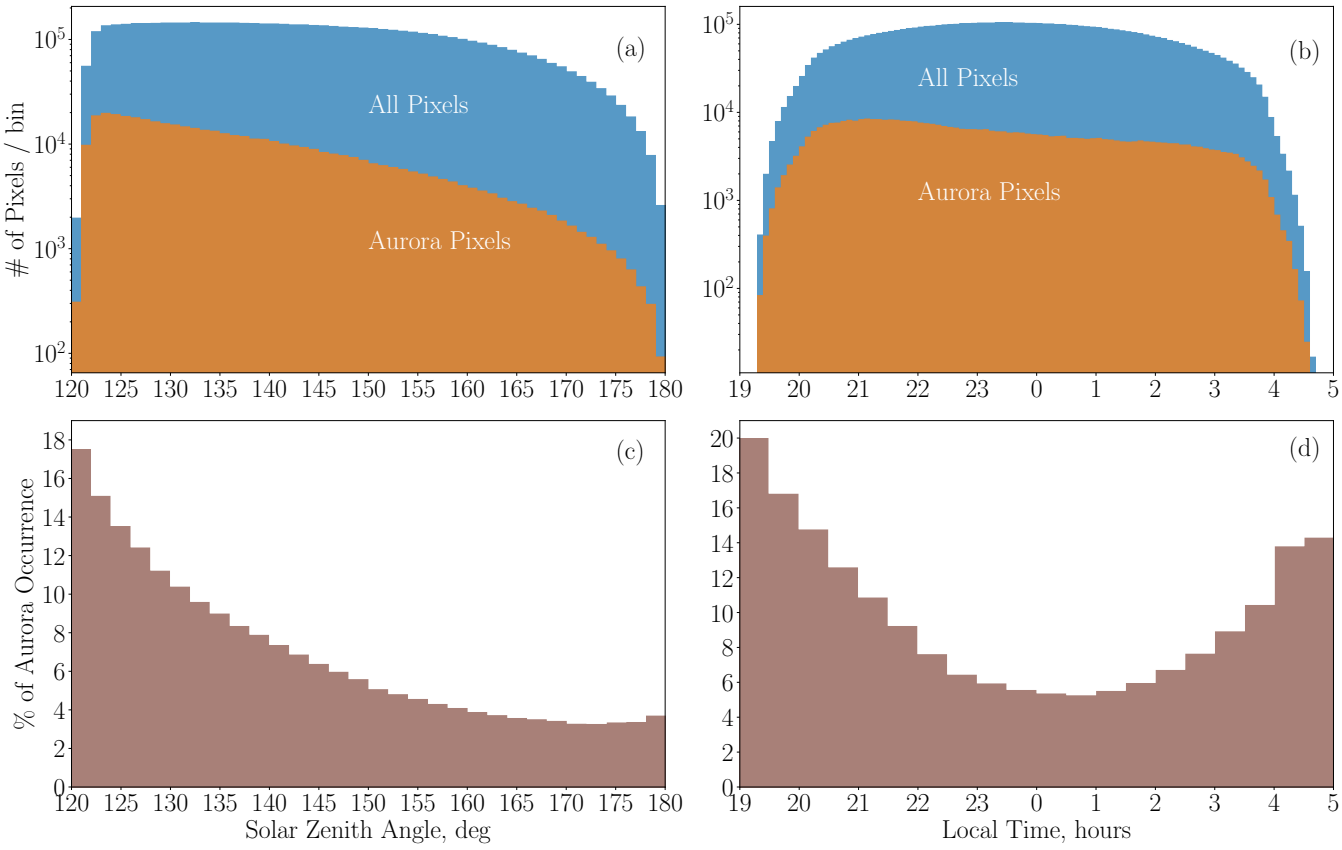

Figure 6. Pixel statistics in solar zenith angle (SZA) and local time bins: a) histogram of all nightside pixels (SZA > 120°) and aurora pixels in SZA bins, and b) histogram of all nightside pixels and aurora pixels in local time bins. Aurora occurrence as a function of c) SZA, and d) local time.

dominates over the crustal magnetic field (Fang et al., 2022). That is, the magnetic field direction at 400 km is less determined by the intrinsic crustal field direction, although, for the auroral emission altitude of ∼130 km, the magnetic field direction is significantly determined by the intrinsic crustal field direction.

4 Solar Zenith Angle and Local Time Variability

The top two panels in Figure 6 show the pixel statistics in SZA (top left panel) and local time bins (top right panel). The blue color histogram corresponds to all nightside pixels and the orange color histogram corresponds to aurora pixels. The bottom panels show the global aurora occurrence, which is calculated as a fraction of aurora pixels to total nightside pixels. Interestingly, aurora shows a SZA dependence, with more aurora occurring close to the terminator as compared to midnight (Figure 6c). This may be attributed to the greater availability of photoelectrons near the terminator compared to the midnight sector. Figure 6d shows the aurora occurrence as a function of local time, and we can notice that there is a dawn–dusk asymmetry, with more aurora occurring in pre–midnight local times as compared to post–midnight local times. This is also consistent with the previous observations by MAVEN IUVS instrument on pre–midnight vs. post–midnight detection frequencies (Johnston et al., 2023; Bowers et al., 2023).

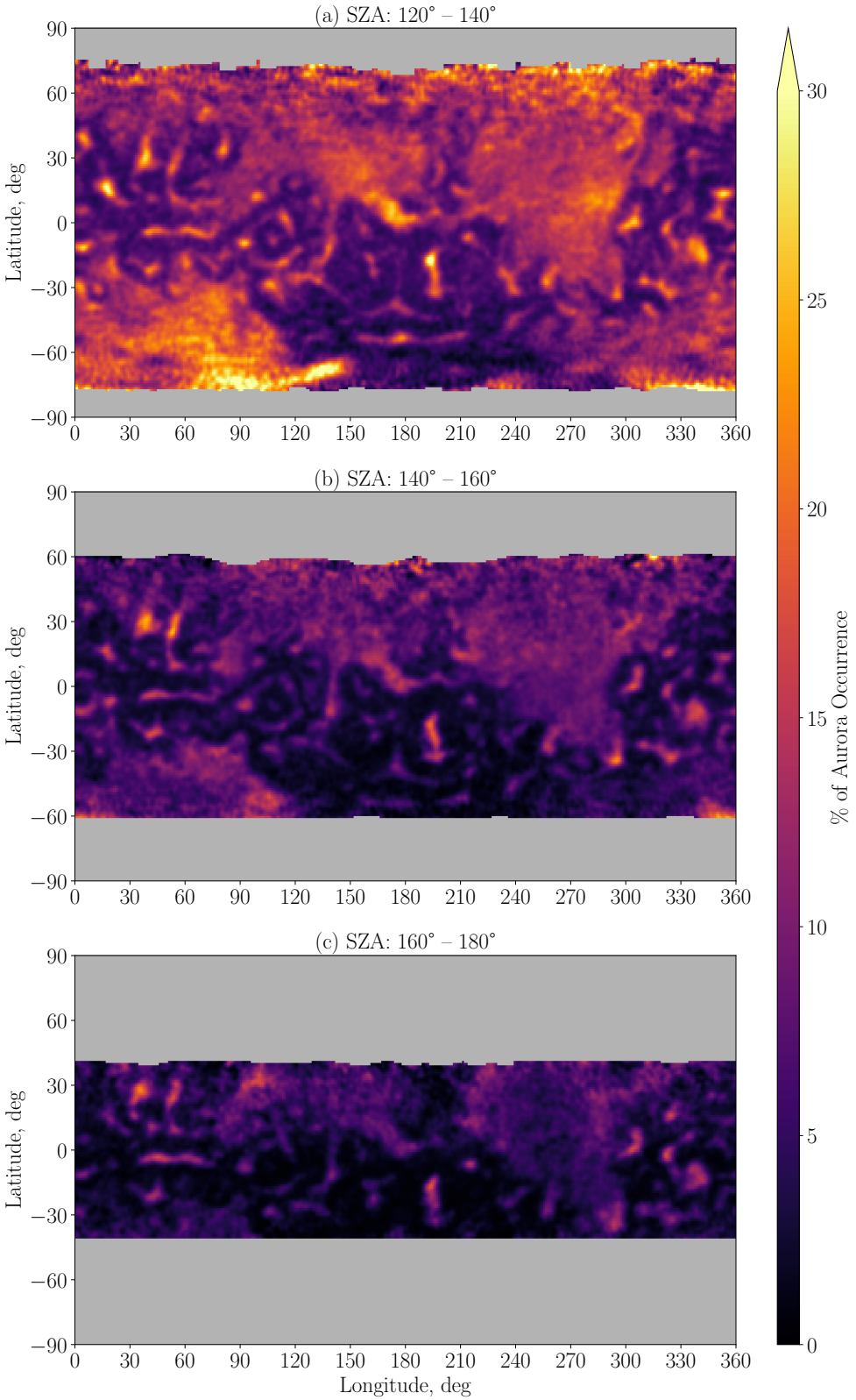

Figure 7. Geographic maps of aurora occurrence (for a brightness threshold of 5 R for OI 130.4 nm emission) for different solar zenith angle (SZA) ranges. a) For SZA from 120 to 140 degrees, b) for SZA from 140 to 160 degrees, and c) for SZA from 160 to 180 degrees.

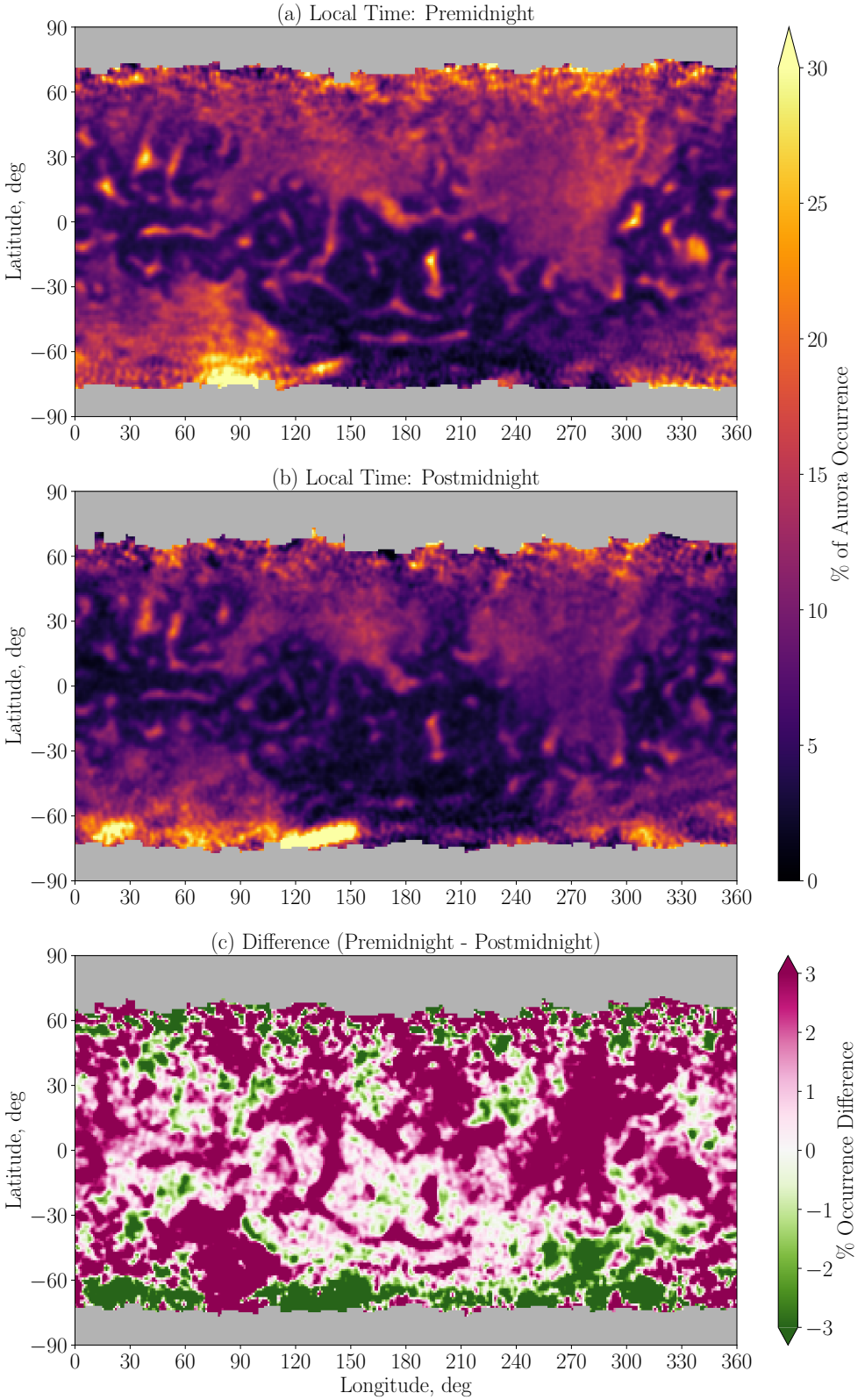

Figure 8. Geographic maps of aurora occurrence (for a brightness threshold of 5 R for OI 130.4 nm emission) for a) pre–midnight (19 - 0 hours) and b) post–midnight (0 - 5 hours) intervals. c) Shows the difference between pre–midnight and post–midnight occurrence rates.

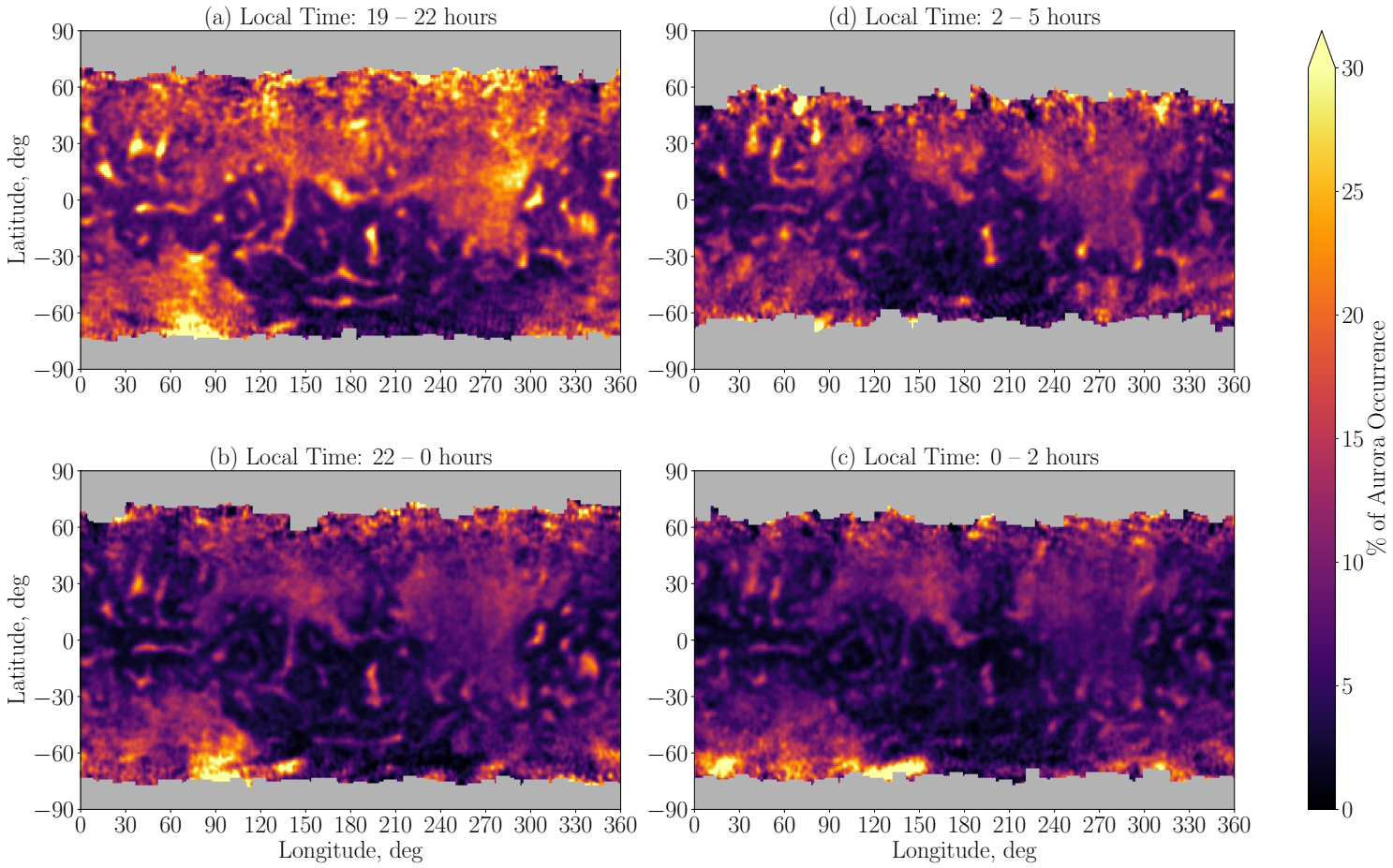

Figure 9. Geographic maps of aurora occurrence (for a brightness threshold of 5 R for OI 130.4 nm emission) for different local time ranges. a) For 19 to 22 hours, b) 22 hours to midnight, c) midnight to 2 hours, and d) 2 to 5 hours. The difference maps comparing these local time bins are provided in Figure S1 of the Supporting Information.

Figure 7 shows the geographic maps of aurora occurrence, similar to Figure 3, but for three different SZA ranges. The first one is for a range 120°–140° (Figure 7a), the second one for 140°–160° (Figure 7b), and the third one for 160°–180° (Figure 7c). Although the nightside geographic coverage reduces for higher SZAs, the aurora occurrence also decreases, as also seen in the histogram (Figure 6c).

Figure 8 shows the geographic maps of aurora occurrence for pre–midnight (19 - 0 hours, Figure 8a) and post–midnight local times (0 - 5 hours, Figure 8b), as well as the map of their difference (Figure 8c). The auroral "spot" in the southern hemisphere mentioned previously is more frequent after midnight than before midnight. Figure 9 shows the geographic maps of aurora occurrence again split into four different local time ranges. As we can see from Figure 6b, the pixel coverage between $\sim$ 19 to 20 hours and $\sim$ 4 to 5 hours is smaller compared to other local time intervals. Hence, we average data from 19 to 22 hours local time for the first subplot of evening or dusk occurrence (Figure 9a), 22 to 0 hours for the second subplot (Figure 9b), 0 to 2 hours for the third subplot (Figure 9c), and 2 to 5 hours for the fourth subplot of morning or dawn occurrence (Figure 9d). The dusk and dawn slices (Figures 9a and 9d) show higher aurora occurrence as compared to the 22 to 2 hours slices (Figures 9b and 9c). Also, the dusk sector has a higher occurrence as compared to the dawn sector.

The geographic maps of percentage difference in aurora occurrence for these four different local time ranges are shown Figure S1 of the Supporting Information. Figure S1a shows the difference between dusk (19 - 22 hours) and dawn (2 - 5 hours) local times, and Figure S1b shows the difference between pre–midnight (22 - 0 hours) and post–midnight (0 - 2 hours) local times. Different regions on the planet (e.g., the strong crustal field region in the southern hemisphere) exhibit a local time dependence with north/south (dusk/dawn) and east/west (pre–midnight/post–midnight) preferred activations (Figures 8c, S1a, S1b), possibly related to the different magnetic field configurations at these locations.

The aurora detections and field line configuration of the strong crustal field region region in the southern hemisphere have been studied recently using MAVEN/IUVS and MAVEN/MAG observations by Johnston et al. (2023) and Bowers et al. (2023). They examined the local time control of aurora observations in the"mini–magnetosphere" region. They found a north/south local time dependence of aurora detections, and attributed this to the magnetic reconnection between crustal fields and draped Interplanetary Magnetic Field (IMF). This interaction between crustal field and draped interplanetary field is found to be different during evening and morning local times (Bowers et al., 2023). However, these studies were restricted to a small part of the strong crustal field region where the fields were oriented north/south.

In another previous study on local time effects on Martian aurora, a concentration of inverted–V auroral particle acceleration events to midnight, with a significant shift towards pre–midnight at Mars was observed by Lundin, Winningham, Barabash, Frahm, Brain, et al. (2006) using ASPERA-3 (Analyzer of Space Plasma and Energetic Atoms)/MEX observations. Also, for comparison, the OI 130.4 nm emission in the Venus aurora was previously observed by the Pioneer Venus Orbiter (PVO) UV spectrometer (Phillips et al., 1986). They observed a typical aurora intensity of 10–20 R, occasionally exceeding 100 R, and have a dawn–dusk asymmetry in brightness, with higher brightness in the evening local time (Phillips et al., 1986).

5 Seasonal Variability

Figure 10 shows the seasonal change of aurora occurrence during MY 36 and early MY 37. The top panel shows aurora occurrence as a function of L_S and latitude, and the bottom panel shows the aurora occurrence as a function of L_S averaged over all geographic locations. The red curve in the bottom panel (Figure 10b) shows the averaged Total Electron Content

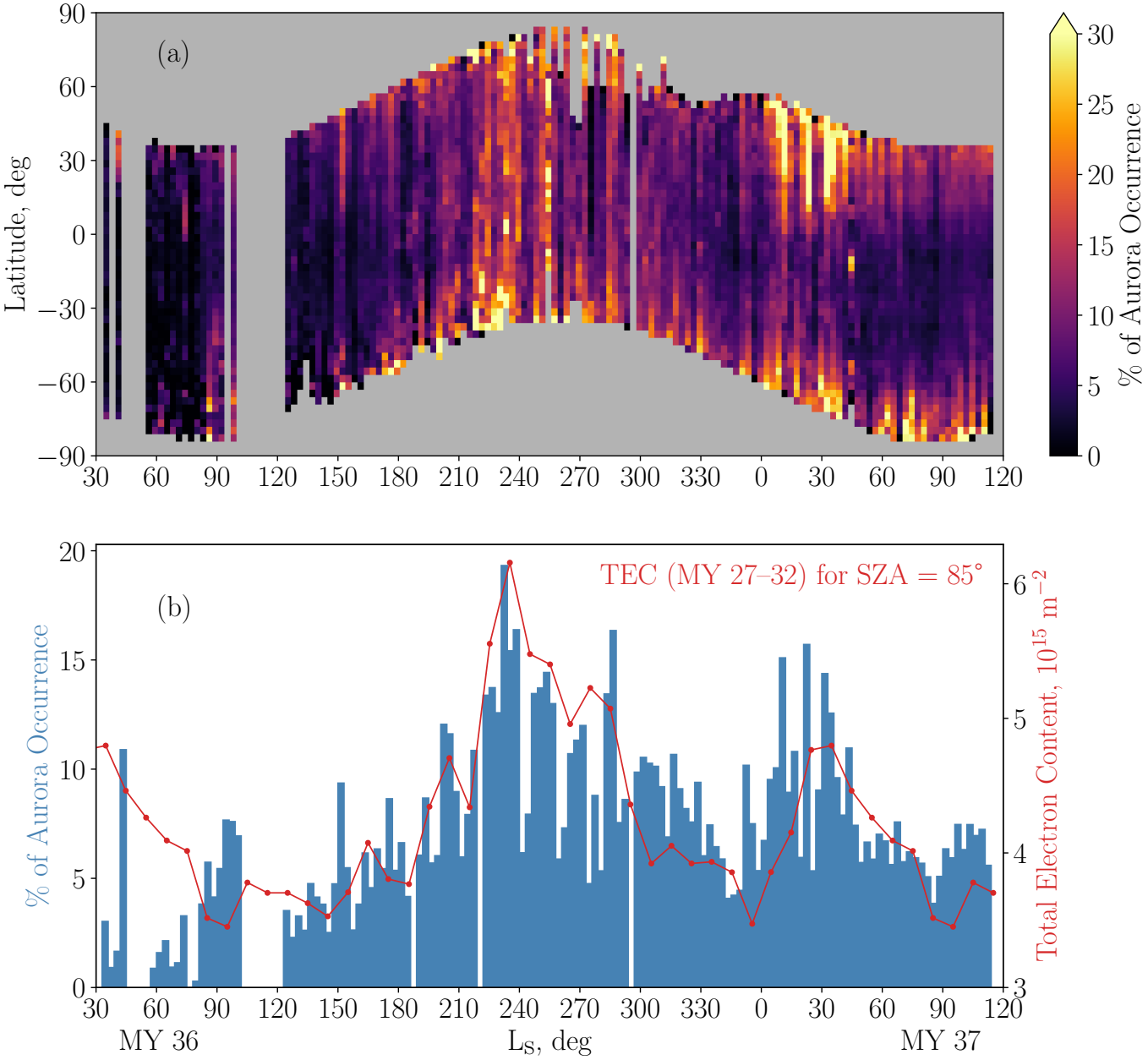

Figure 10. Seasonal variability of aurora occurrence (for a brightness threshold of 5 R for OI 130.4 nm emission), a) as a function of L_S and latitude, b) as a function of L_S averaged over all geographic locations. The red curve in panel (b) shows the averaged Total Electron Content (TEC) from Mars Express MARSIS for MY 27–32 and for SZA = 85° digitized from Sánchez-Cano et al. (2018).

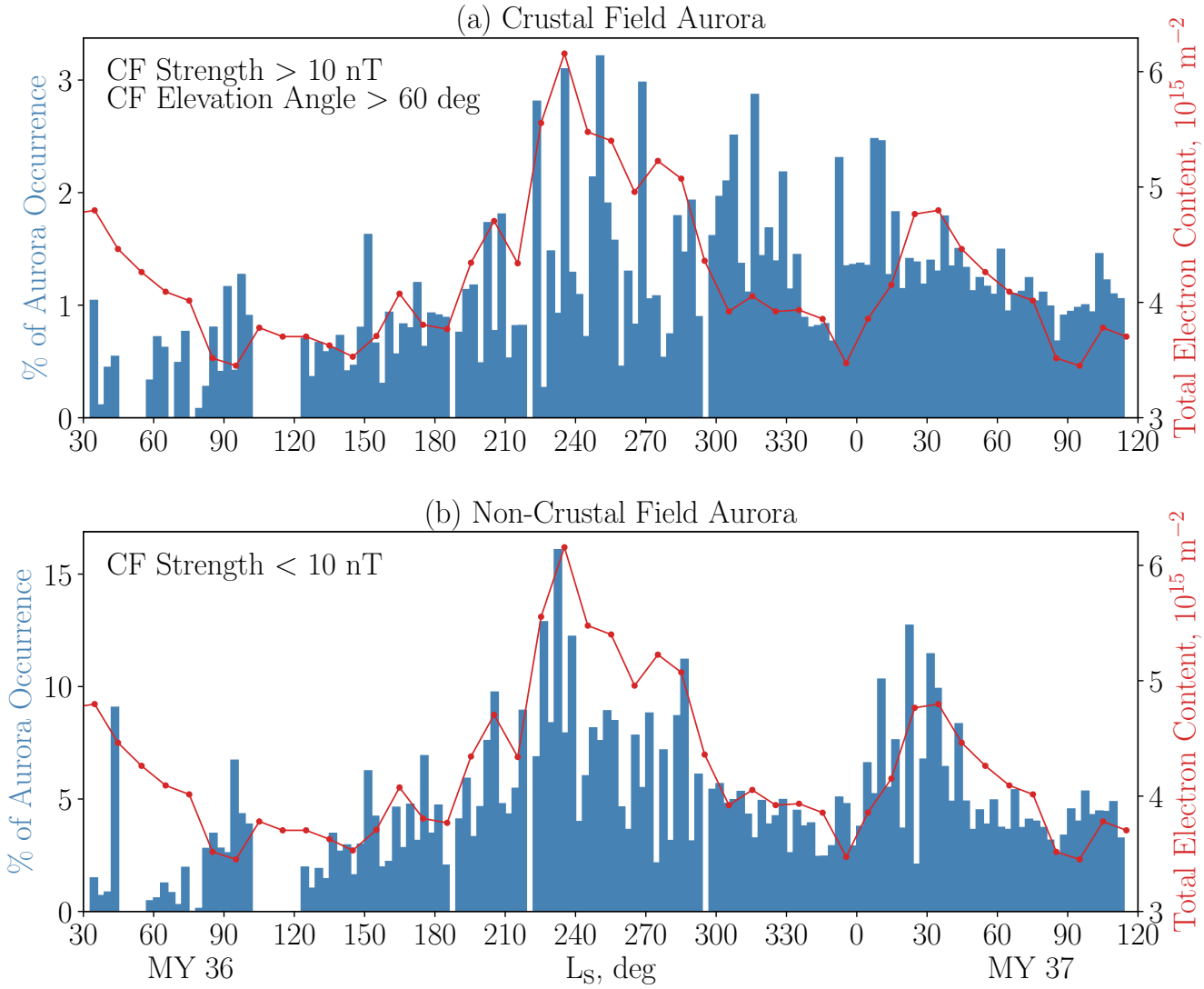

Figure 11. Seasonal variability of aurora occurrence as a function of L_S averaged over all geographic locations and divided into a) crustal field aurora (crustal field strength at 400 km greater than 10 nT and elevation angle greater than 60°), b) non–crustal field aurora (crustal field strength at 400 km less than 10 nT). The red curve in both panels show the averaged Total Electron Content (TEC) from Mars Express MARSIS for MY 27–32 and for SZA = 85° digitized from Sánchez-Cano et al. (2018).

(TEC) from Mars Express (MEX) Mars Advanced Radar for Subsurface and Ionospheric Sounding (MARSIS) for MY 27–32 and for SZA = 85° (digitized data from Figure 1 of Sánchez-Cano et al. (2018)). It is interesting to see that two distinct enhancements in aurora occurrence is observed, the primary enhancement from $\sim$ 210 to 300 degrees L_S and the secondary peak from $\sim$ 0 to 60 degrees L_S. This is matching with the primary and secondary enhancements identified in the ionospheric TEC measured by MARSIS. The annual occurrence of both TEC maxima in MARSIS data was found to be independent of solar conditions, such as the SZA or solar activity. Sánchez-Cano et al. (2018) attributed the variability in solar irradiance (peaking near perihelion) as the cause for the primary enhancement, while the second peak is not related to the solar irradiance variation but instead coincides with an increase in the thermospheric density. The thermospheric density increase is possibly linked to the variation in surface pressure produced by atmospheric cycles such as the CO_2 or water cycles (Sánchez-Cano et al., 2018). This suggests a relationship between the ionospheric photoelectron content near–terminator and the nightside discrete aurora. As the Solar Cycle 25 ramped up further in MY 37 (increased solar activity, solar irradiance and hence a denser ionosphere (Sánchez-Cano et al., 2016)), the aurora activity also increased as compared to MY 36 (Figure 10).

Additionally, we split the histogram of seasonal dependence based on the crustal field strength as Crustal Field Aurora (Figure 11a) and Non–Crustal Field Aurora (Figure 11b). We can see that the global occurrence rate of non–crustal field aurora is higher than the global occurrence rate of crustal field aurora. Also, non–crustal field aurora follows the Total Electron Content (TEC) variation, but the crustal field aurora is not exactly following the TEC variation, although the increased occurrence during perihelion season and increase with solar activity progression is evident in the crustal field aurora as well. Hence, we propose that the non–crustal field aurora (predominantly the patchy non–crustal field aurora) is primarily contributed by the impact of ionospheric photoelectrons, while the source of crustal field aurora could be more energetic electrons, for example those from the magnetosphere or the solar wind or the low–energy electrons (such as photoelectrons) accelerated downward in crustal field cusp by parallel potentials or energization of low–energy electrons due to magnetic reconnection and plasma waves (Lundin, Winningham, Barabash, Frahm, Holmström, et al., 2006; Brain, 2006; Fang et al., 2022). The denser ionosphere near perihelion is a potential source of electrons for these acceleration mechanisms, and thus the crustal field aurora as well.

Variability of aurora occurrence as a function of subsolar longitude (which is analogous to local time) and subsolar latitude (which is analogous to seasons on Mars) is shown in Figure S2 of the Supporting Information.

6 Aurora Brightness Variability

Figure 12 shows the geographic maps of OI 130.4 nm aurora emission brightness. Figure 12a shows the mean brightness in 1° by 1° geographic bins. Figure 12b shows the standard deviation of the samples in each bin, and Figure 12c shows the ratio of mean brightness and standard deviation in each geographic bin. Bright aurorae generally occur in strong vertical crustal field regions (although some of the brightest regions are also the most variable), including the mini–magnetosphere in the southern hemisphere. However, we can also see the signature of just a few bright instances of sinuous aurora in the northern hemisphere. A total of fewer than 100 sinuous aurora events have been detected by EMUS so far, and these are analyzed in another study.

Figure 13a shows the seasonal variation of aurora brightness for MY 36 and MY 37. Prominent bright patches corresponds to bright aurora events (often associated with solar transient events such as Coronal Mass Ejections (CMEs) and Stream Interaction Regions (SIRs)). Previously, Brain (2006) suggested that most energetic auroral particle acceleration events are likely to be observed during periods of disturbed solar wind conditions, such as

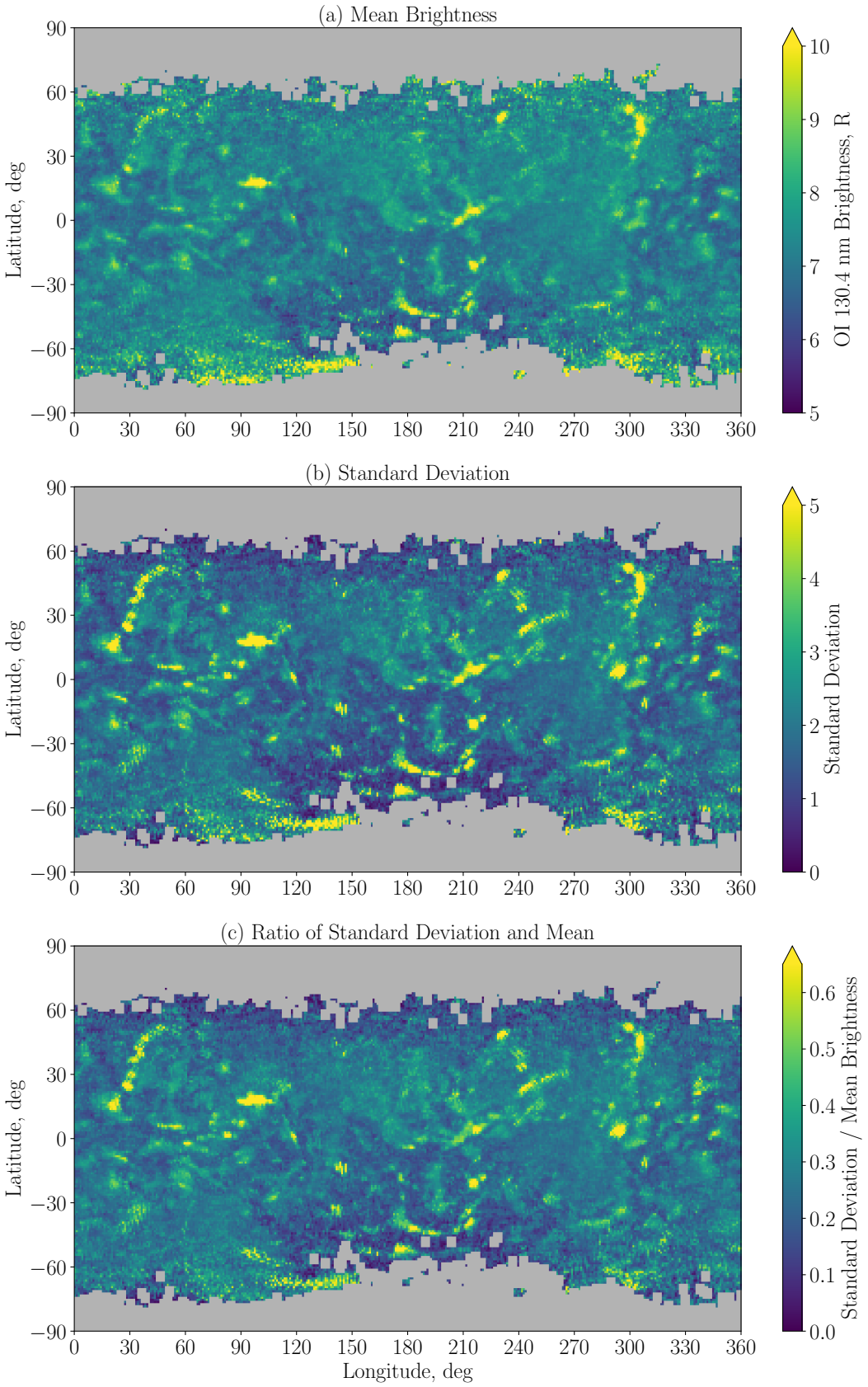

Figure 12. Geographic maps of a) mean aurora brightness of OI 130.4 nm emission, b) standard deviation of the population, and c) ratio of standard deviation and mean brightness.

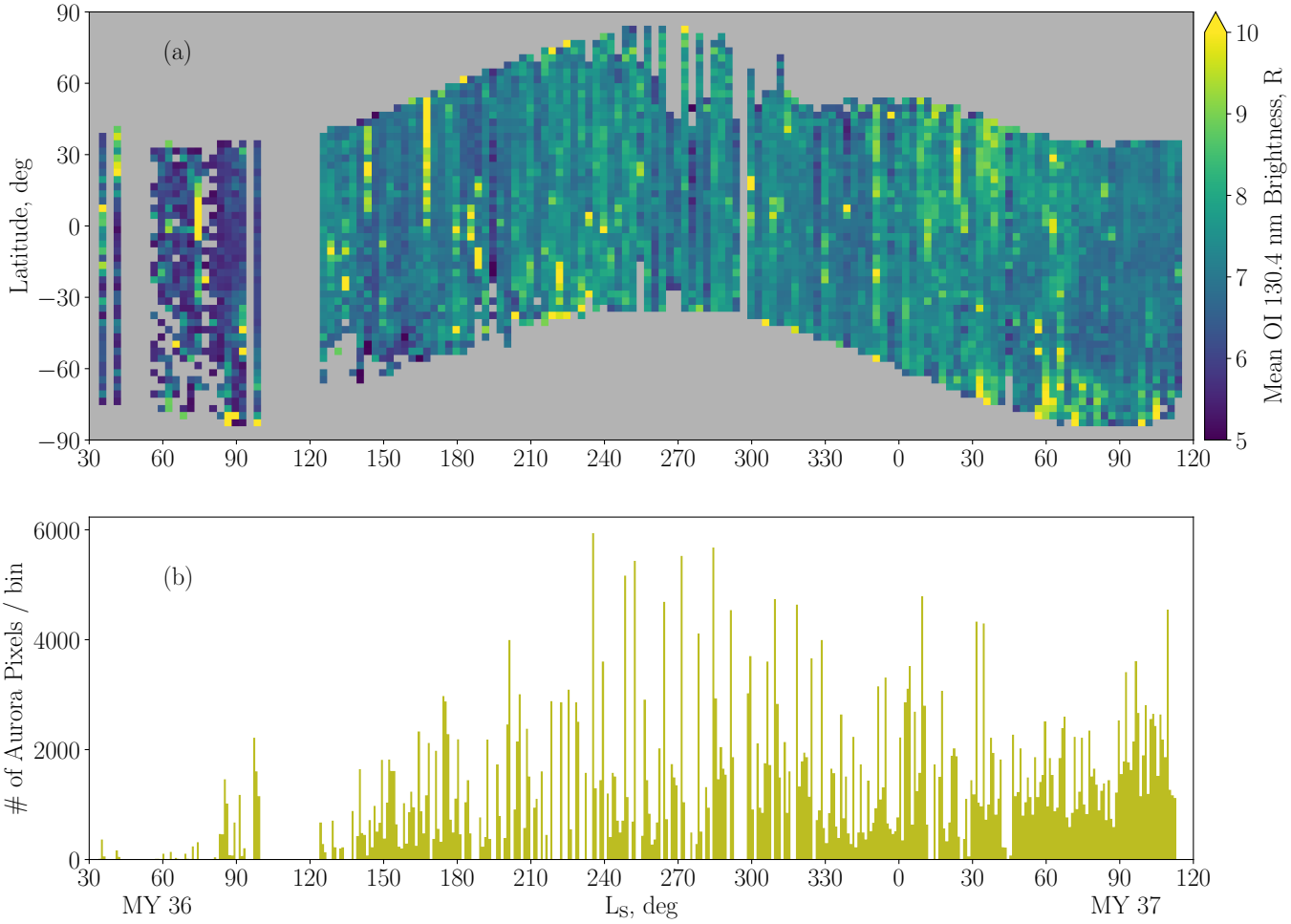

Figure 13. a) Seasonal variability of mean aurora brightness of OI 130.4 nm emission as a function of L_S and latitude, and b) histogram showing the number of aurora pixels (brightness threshold of 5 R) as a function of L_S. We can notice that the total number of aurora pixels follows the seasonal variability shown in Figures 10 and 11. We can also notice that the aphelion season of MY 37 has more aurora than the aphelion season of MY 36 due to increased solar activity (i.e., due to the inclining phase of Solar Cycle 25).

CMEs. The Venus aurora observations also suggested increased aurora brightness in OI 130.4 nm during interplanetary shock events (Phillips et al., 1986).

Nevertheless, we note that the seasonal trend in aurora occurrence is also seen in aurora brightness. Figure 13b shows the number of aurora pixels as a function of Martian season. We can notice the seasonal enhancements during perihelion (near L_S 235°) and near L_S 30°. The earlier period of MY 36 was mostly quiet (except the occasional bright aurora due to transient events, example on 2021/07/21), and the brightness is prominently increased for $\sim$ 210 to 300 degrees L_S and $\sim$ 0 to 60 degrees L_S, primarily contributed by the non–crustal field patchy aurora due to an increase in the source photoelectrons. Solar Cycle 25 is rising, and the solar activity is observed to have an effect on observed auroral brightness. We can notice this solar activity enhancement in auroral brightness when comparing the aphelion seasons of MY 36 and MY 37 (Figure 13). The dependence of discrete aurora occurrence and brightness levels on upstream solar wind and Interplanetary Magnetic Field (IMF) conditions will be examined in a separate paper.

7 Photoelectron precipitation on the nightside is a significant contributor to discrete aurora

The first measurements of discrete aurora by MEX/SPICAM were carried out in the strong crustal field region in the southern hemisphere, where the field lines are more likely open and are vertical, analogous to the terrestrial polar cusps (Lundin, Winningham, Barabash, Frahm, Brain, et al., 2006; Brain et al., 2006). Also, peaked electron energy distributions were observed, very similar to the "inverted–V" structures (characterized by downward traveling electrons and upward traveling planetary ions) similar to aurora on Earth (Lundin, Winningham, Barabash, Frahm, Holmström, et al., 2006; Brain et al., 2006; Dubinin et al., 2008; Lundin, Winningham, Barabash, Frahm, Brain, et al., 2006; Bisikalo et al., 2017). Quasi–static field–aligned potential could be one mechanism that accelerate electrons and ions (Lundin, Winningham, Barabash, Frahm, Brain, et al., 2006; Brain & Halekas, 2012). These accelerated down–going electrons encounter the atmosphere and lead to both enhanced ionization and auroral emission (Fillingim et al., 2007; Lillis & Brain, 2013).

Leblanc et al. (2006) simulated the emission rate of this aurora due to electron precipitation, and suggested that the measured emissions might have been produced by electrons of a few tens of eV rather than by the electrons of above 100 eV. Leblanc et al. (2008) showed a correlation between the auroral emissions observed by SPICAM and electron flux observed by Analyzer of Space Plasma and Energetic Atoms (ASPERA-3) Electron Spectrometer as well as with the Total Electron Content (TEC) observed by Mars Advanced Radar for Subsurface and Ionosphere Sounding (MARSIS) in subsurface mode – using the ionospheric phase distortion to the radio signal. Clear peak in TEC during the time of SPICAM measurement of the auroral events was noted (Leblanc et al., 2008). Hence, photoelectron transport to the nightside and acceleration by quasi–static field–aligned potentials above crustal field cusp were seemed to be the processes responsible for the observed aurora emissions. Other proposed mechanisms for electron acceleration include magnetic reconnection, plasma waves and current sheet on the nightside (Brain & Halekas, 2012; Bowers et al., 2023; Uluşen & Linscott, 2008; J. S. Halekas et al., 2006; J. Halekas et al., 2008). Lillis et al. (2022) suggested that sinuous non–crustal field aurora observed by EMUS could be due to accelerated electrons in the magnetotail current sheet, which is consistent with the previous observations of magnetotail current sheet extending to very low altitudes on the nightside, and those were not associated with crustal fields (J. S. Halekas et al., 2006).

MAVEN Solar Wind Electron Analyzer (SWEA) has also measured electron energy and pitch angle distributions to study the accelerated electron populations associated with discrete aurora (Xu et al., 2020). These auroral electron events share the same characteristics such as location, crustal field, etc. as the MAVEN/IUVS observed auroral emission events,

thus establishing a causal connection (Xu et al., 2022). MAVEN/SWEA observations also revealed the spectral features of accelerated electron populations which suggest that they originate from a cold plasma with electron temperature as low as 1 eV like the thermal ionosphere (Akbari et al., 2019). Fang et al. (2022) used global plasma modeling to predict aurora occurrence location and probability. They found aurora occurs more likely on small–scale patches inside strong crustal field regions, and also occurrence increases during space weather events (Fang et al., 2022).

The modeling study by Fox and Stewart (1991) suggested that precipitation of very soft electrons into the nightside Venusian atmosphere as the source of aurora. From Mars Express data, low–energy electrons appear to be responsible for a subset of aurora observations, and it is therefore expected that transport of electrons from day to night should occur (Liemohn et al., 2007; Brain & Halekas, 2012; Liemohn et al., 2006). The dayside ionospheric photoelectrons have nearly the appropriate energy distribution (tens of eV) to explain the auroral emission, and could be due to photoelectrons transported from day to night across the terminator (Leblanc et al., 2006; Bertaux et al., 2005; Leblanc et al., 2008), and photoelectrons have been observed well above the ionosphere of Mars (Frahm et al., 2006; Frahm et al., 2006). MAVEN/SWEA also observed photoelectrons deep on the nightside due to day–night magnetic connectivity allowing cross–terminator transport of electrons (Xu et al., 2016).

The seasonal variability of discrete aurora occurrence and brightness presented here demonstrates for the first time that the aurora follows the variation in ionospheric photoelectrons. This further supports the hypothesis that photoelectron precipitation is a significant contributor to discrete aurora on Mars, especially the patchy non–crustal field aurora.

8 Conclusions and Future Prospects

The wealth of new synoptic images from EMUS onboard EMM provides unprecedented observations of the nightside discrete electron aurora on Mars. Our statistical analysis of these synoptic images reveals the following:

1. Aurora shows a geographic preference, with a higher aurora occurrence in regions having open magnetic topology and strong vertical crustal fields. Aurora voids are observed in areas where electron precipitation is blocked by closed crustal magnetic field loops.
2. Higher aurora occurrence is observed near the terminator sector as compared to the midnight sector. There is a dawn–dusk asymmetry, with a greater occurrence of aurora in pre–midnight local times (evening) than in post–midnight local times (morning). This confirms the dawn–dusk asymmetry in aurora detections observed by MAVEN spacecraft (Johnston et al., 2023; Schneider et al., 2021). Distinct local time–dependent electron features (such as the electron "spot" in the southern hemisphere) previously observed by MGS (Brain et al., 2007), are also evident in EMUS auroral observations.
3. Aurora shows a seasonal dependence, with a primary enhancement near L_S 235° and a secondary enhancement near L_S 30°. Both enhancements are consistent with the seasonal variability of near–terminator ionospheric TEC observed by MARSIS onboard MEX, which in turn depends on the solar irradiance and thermospheric density (Sánchez-Cano et al., 2018), implying a photoelectron source for discrete aurora. Aurora occurrence also shows an increase with increasing solar activity due to the rise of Solar Cycle 25.
4. Classifying the seasonal variability of aurora into crustal field aurora and non–crustal field aurora reveals that the seasonal peaks are more prominent for the non–crustal field aurora, primarily contributed by the patchy non–crustal field aurora. However, the perihelion season enhancement in occurrence is also evident for crustal field aurora.

5. Aurora brightness shows a geographic distribution, with brighter features appearing in the strong crustal field regions (due to crustal field aurora), as well as in the northern hemisphere (with signatures of non–crustal field sinuous aurora). Aurora brightness also shows a seasonal and solar cycle variability similar to aurora occurrence.

Further comparative studies are required to understand the dependence of aurora occurrence on varying magnetic field topologies, as the topology varies with altitude, local time, season, IMF polarity, etc. (Xu et al., 2017, 2019; Brain et al., 2020; Weber et al., 2017, 2020; Fang et al., 2022). The auroral electron energy distribution can be better constrained using the ratio of oxygen auroral emissions OI 130.4 nm and OI 135.6 nm (Fox & Stewart, 1991). As mentioned previously, dependence of aurora on upstream solar wind parameters and IMF parameters also needs to be examined (Girazian et al., 2022; Schneider et al., 2021). Furthermore, the mechanisms for particle precipitation and aurora formation require detailed exploration (Bowers et al., 2023; Haider et al., 2022; Brain & Halekas, 2012). The consequences of aurora, such as enhanced ionization (creating a "patchy" ionosphere), Joule heating of the upper atmosphere, changes in chemical composition, and enhanced ion escape via auroral flux tubes, need further investigation (Fillingim et al., 2007; Shematovich et al., 2017; Brain & Halekas, 2012).

In summary, the insights gathered from EMM/EMUS observations not only advances our understanding of Martian discrete aurora but also sets the stage for future explorations that promise to unravel the complex interplay between Sun's activity, Martian magnetic fields, ionospheric and magnetospheric dynamics. This endeavor will not only enhance our knowledge of Mars' present–day environment but also contribute to our broader understanding of weakly magnetized planetary atmospheres and their interactions with space weather.

Open Research Section

Data Availability Statement

The EMM/EMUS l2a data we analyze here are available at the EMM Science Data Center (SDC, `https://sdc.emiratesmarsmission.ae/`). This location is designated as the primary repository for all data products produced by the EMM team and is designated as long–term repository as required by the UAE Space Agency. The data available (`https://sdc.emiratesmarsmission.ae/data`) include ancillary spacecraft data, instrument telemetry, Level 1 (raw instrument data) to Level 3 (derived science products), quicklook products, and data users guides (`https://sdc.emiratesmarsmission.ae/documentation`) to assist in the analysis of the data. Following the creation of a free login, all EMM data are searchable via parameters such as product file name, solar longitude, acquisition time, sub-spacecraft latitude and longitude, instrument, data product level, etc. EMUS data and users guides are available at: `https://sdc.emiratesmarsmission.ae/data/emus`.

Acknowledgments

Funding for development of the EMM mission is provided by the UAE government, and to co–authors outside of the UAE by MBRSC. KC and RS are supported by the grant 8474000332-KU-CU-LASP Space Sci. XF is supported by NASA Grant 80NSSC19K0562.

References

Akbari, H., Andersson, L., Fowler, C., & Mitchell, D. (2019). Spectral Analysis of Accelerated Electron Populations at Mars. *Journal of Geophysical Research: Space Physics*, *124*(10), 8056-8065. Retrieved from `https://agupubs.onlinelibrary.wiley.com/doi/abs/10.1029/2019JA026738` doi: https://doi.org/10.1029/2019JA026738

Almatroushi, H., AlMazmi, H., AlMheiri, N., AlShamsi, M., AlTunaiji, E., Badri, K., ... Young, R. M. B. (2021, December). Emirates Mars Mission Characterization of

Mars Atmosphere Dynamics and Processes. *Space Science Reviews*, *217*(8), 89. doi: 10.1007/s11214-021-00851-6

Amiri, H. E. S., Brain, D., Sharaf, O., Withnell, P., McGrath, M., Alloghani, M., ... Yousuf, M. (2022, February). The Emirates Mars Mission. *Space Science Reviews*, *218*(1), 4. doi: 10.1007/s11214-021-00868-x

Atri, D., Dhuri, D. B., Simoni, M., & Sreenivasan, K. R. (2022, December). Auroras on Mars: From discovery to new developments. *European Physical Journal D*, *76*(12), 235. doi: 10.1140/epjd/s10053-022-00566-5

Bertaux, J.-L., Korablev, O., Perrier, S., Quémerais, E., Montmessin, F., Leblanc, F., ... Guibert, S. (2006). SPICAM on Mars Express: Observing modes and overview of UV spectrometer data and scientific results. *Journal of Geophysical Research: Planets*, *111*(E10). Retrieved from `https://agupubs.onlinelibrary.wiley.com/doi/abs/10.1029/2006JE002690` doi: https://doi.org/10.1029/2006JE002690

Bertaux, J.-L., Leblanc, F., Witasse, O., Quemerais, E., Lilensten, J., Stern, S. A., ... Korablev, O. (2005, June). Discovery of an aurora on Mars. *Nature*, *435*(7043), 790-794. doi: 10.1038/nature03603

Bisikalo, D., Shematovich, V., Gérard, J.-C., & Hubert, B. (2017). Influence of the crustal magnetic field on the Mars aurora electron flux and UV brightness. *Icarus*, *282*, 127-135. Retrieved from `https://www.sciencedirect.com/science/article/pii/S0019103516305504` doi: https://doi.org/10.1016/j.icarus.2016.08.035

Bowers, C. F., DiBraccio, G. A., Slavin, J. A., Johnston, B., Schneider, N. M., Brain, D. A., & Azari, A. (2023). Evidence for Magnetic Reconnection as the Precursor to Discrete Aurora at Mars. *Journal of Geophysical Research: Space Physics*, *128*(12), e2023JA031622. Retrieved from `https://agupubs.onlinelibrary.wiley.com/doi/abs/10.1029/2023JA031622` (e2023JA031622 2023JA031622) doi: https://doi.org/10.1029/2023JA031622

Brain, D., & Halekas, J. S. (2012). Aurora in Martian Mini Magnetospheres. In *Auroral Phenomenology and Magnetospheric Processes: Earth And Other Planets* (p. 123-132). American Geophysical Union (AGU). Retrieved from `https://agupubs.onlinelibrary.wiley.com/doi/abs/10.1029/2011GM001201` doi: https://doi.org/10.1029/2011GM001201

Brain, D. A. (2006, October). Mars Global Surveyor Measurements of the Martian Solar Wind Interaction. *Space Science Reviews*, *126*(1-4), 77-112. doi: 10.1007/s11214-006-9122-x

Brain, D. A., Halekas, J. S., Peticolas, L. M., Lin, R. P., Luhmann, J. G., Mitchell, D. L., ... Rème, H. (2006). On the origin of aurorae on Mars. *Geophysical Research Letters*, *33*(1). Retrieved from `https://agupubs.onlinelibrary.wiley.com/doi/abs/10.1029/2005GL024782` doi: https://doi.org/10.1029/2005GL024782

Brain, D. A., Lillis, R. J., Mitchell, D. L., Halekas, J. S., & Lin, R. P. (2007). Electron pitch angle distributions as indicators of magnetic field topology near Mars. *Journal of Geophysical Research: Space Physics*, *112*(A9). Retrieved from `https://agupubs.onlinelibrary.wiley.com/doi/abs/10.1029/2007JA012435` doi: https://doi.org/10.1029/2007JA012435

Brain, D. A., Weber, T., Xu, S., Mitchell, D. L., Lillis, R. J., Halekas, J. S., ... Jakosky, B. M. (2020). Variations in Nightside Magnetic Field Topology at Mars. *Geophysical Research Letters*, *47*(19), e2020GL088921. Retrieved from `https://agupubs.onlinelibrary.wiley.com/doi/abs/10.1029/2020GL088921` (e2020GL088921 2020GL088921) doi: https://doi.org/10.1029/2020GL088921

Chaffin, M. S., Fowler, C. M., Deighan, J., Jain, S., Holsclaw, G., Hughes, A., ... AlMatroushi, H. (2022). Patchy Proton Aurora at Mars: A Global View of Solar Wind Precipitation Across the Martian Dayside From EMM/EMUS. *Geophysical Research Letters*, *49*(17), e2022GL099881. Retrieved from `https://agupubs.onlinelibrary.wiley.com/doi/abs/10.1029/2022GL099881` (e2022GL099881 2022GL099881) doi: https://doi.org/10.1029/2022GL099881

Chirakkil, K., Deighan, J., Chaffin, M. S., Jain, S. K., Lillis, R. J., Susarla, R., ... Curry,

S. (2023). EMM EMUS Observations of Hot Oxygen Corona at Mars: Radial Distribution and Temporal Variability. *Journal of Geophysical Research: Space Physics*, accepted. Retrieved from https://doi.org/10.22541/essoar.170224474.48958302/v1 doi: 10.1029/2023JA032342

Deighan, J., Jain, S. K., Chaffin, M. S., Fang, X., Halekas, J. S., Clarke, J. T., ... Jakosky, B. M. (2018, July). Discovery of a proton aurora at Mars. *Nature Astronomy*, *2*, 802-807. doi: 10.1038/s41550-018-0538-5

Dubinin, E., Fraenz, M., Woch, J., Winnigham, J., Frahm, R., Lundin, R., & Barabash, S. (2008). Suprathermal electron fluxes on the nightside of Mars: ASPERA-3 observations. *Planetary and Space Science*, *56*(6), 846-851. Retrieved from https://www.sciencedirect.com/science/article/pii/S0032063307003893 (Mars Express/Venus Express) doi: https://doi.org/10.1016/j.pss.2007.12.010

England, S. L., Jain, S., Deighan, J., Chaffin, M., Holsclaw, G., Evans, J. S., ... Almazmi, H. (2022). Spatio-Temporal Structure of Far Ultraviolet Martian Dayglow Observed by EMM-EMUS. *Geophysical Research Letters*, *49*(19), e2022GL099611. Retrieved from https://agupubs.onlinelibrary.wiley.com/doi/abs/10.1029/2022GL099611 (e2022GL099611 2022GL099611) doi: https://doi.org/10.1029/2022GL099611

Fang, X., Ma, Y., Schneider, N., Girazian, Z., Luhmann, J., Milby, Z., ... Jakosky, B. (2022). Discrete Aurora on the Nightside of Mars: Occurrence Location and Probability. *Journal of Geophysical Research: Space Physics*, *127*(3), e2021JA029716. Retrieved from https://agupubs.onlinelibrary.wiley.com/doi/abs/10.1029/2021JA029716 (e2021JA029716 2021JA029716) doi: https://doi.org/10.1029/2021JA029716

Fillingim, M. O., Peticolas, L. M., Lillis, R. J., Brain, D. A., Halekas, J. S., Mitchell, D. L., ... Kirchner, D. L. (2007). Model calculations of electron precipitation induced ionization patches on the nightside of Mars. *Geophysical Research Letters*, *34*(12). Retrieved from https://agupubs.onlinelibrary.wiley.com/doi/abs/10.1029/2007GL029986 doi: https://doi.org/10.1029/2007GL029986

Fox, J. L., & Stewart, A. I. F. (1991). The Venus ultraviolet aurora: A soft electron source. *Journal of Geophysical Research: Space Physics*, *96*(A6), 9821-9828. Retrieved from https://agupubs.onlinelibrary.wiley.com/doi/abs/10.1029/91JA00252 doi: https://doi.org/10.1029/91JA00252

Frahm, R., Winningham, J., Sharber, J., Scherrer, J., Jeffers, S., Coates, A., ... Dierker, C. (2006). Carbon dioxide photoelectron energy peaks at Mars. *Icarus*, *182*(2), 371-382. Retrieved from https://www.sciencedirect.com/science/article/pii/S0019103506000352 (Results from the Mars Express ASPERA-3 Investigation) doi: https://doi.org/10.1016/j.icarus.2006.01.014

Frahm, R. A., Sharber, J. R., Winningham, J. D., Wurz, P., Liemohn, M. W., Kallio, E., ... Mckenna-Lawler, S. (2006, October). Locations of Atmospheric Photoelectron Energy Peaks Within the Mars Environment. *Space Science Reviews*, *126*(1-4), 389-402. doi: 10.1007/s11214-006-9119-5

Gérard, J. C., Hubert, B., Ritter, B., Shematovich, V. I., & Bisikalo, D. V. (2019, March). Lyman-α emission in the Martian proton aurora: Line profile and role of horizontal induced magnetic field. *Icarus*, *321*, 266-271. doi: 10.1016/j.icarus.2018.11.013

Gérard, J.-C., Soret, L., Libert, L., Lundin, R., Stiepen, A., Radioti, A., & Bertaux, J.-L. (2015). Concurrent observations of ultraviolet aurora and energetic electron precipitation with Mars Express. *Journal of Geophysical Research: Space Physics*, *120*(8), 6749-6765. Retrieved from https://agupubs.onlinelibrary.wiley.com/doi/abs/10.1002/2015JA021150 doi: https://doi.org/10.1002/2015JA021150

Gérard, J.-C., Soret, L., Shematovich, V., Bisikalo, D., & Bougher, S. (2017). The Mars diffuse aurora: A model of ultraviolet and visible emissions. *Icarus*, *288*, 284-294. Retrieved from https://www.sciencedirect.com/science/article/pii/S0019103516305450 doi: https://doi.org/10.1016/j.icarus.2017.01.037

Girazian, Z., Schneider, N. M., Milby, Z., Fang, X., Halekas, J., Weber, T., ...

Lee, C. O. (2022). Discrete Aurora at Mars: Dependence on Upstream Solar Wind Conditions. *Journal of Geophysical Research: Space Physics*, *127*(4), e2021JA030238. Retrieved from https://agupubs.onlinelibrary.wiley.com/doi/abs/10.1029/2021JA030238 (e2021JA030238 2021JA030238) doi: https://doi.org/10.1029/2021JA030238

Haider, S. A., Mahajan, K. K., Bougher, S. W., Schneider, N. M., Deighan, J., Jain, S. K., & Gérard, J. C. (2022, June). Observations and Modeling of Martian Auroras. *Space Science Reviews*, *218*(4), 32. doi: 10.1007/s11214-022-00906-2

Halekas, J., Brain, D., Lin, R., Luhmann, J., & Mitchell, D. (2008). Distribution and variability of accelerated electrons at Mars. *Advances in Space Research*, *41*(9), 1347-1352. Retrieved from https://www.sciencedirect.com/science/article/pii/S0273117707000476 doi: https://doi.org/10.1016/j.asr.2007.01.034

Halekas, J. S., Brain, D. A., Lillis, R. J., Fillingim, M. O., Mitchell, D. L., & Lin, R. P. (2006). Current sheets at low altitudes in the Martian magnetotail. *Geophysical Research Letters*, *33*(13). Retrieved from https://agupubs.onlinelibrary.wiley.com/doi/abs/10.1029/2006GL026229 doi: https://doi.org/10.1029/2006GL026229

Holsclaw, G. M., Deighan, J., Almatroushi, H., Chaffin, M., Correira, J., Evans, J. S., ... Tyagi, K. (2021, December). The Emirates Mars Ultraviolet Spectrometer (EMUS) for the EMM Mission. *Space Science Reviews*, *217*(8), 79. doi: 10.1007/s11214-021-00854-3

Hughes, A., Chaffin, M., Mierkiewicz, E., Deighan, J., Jain, S., Schneider, N., ... Jakosky, B. (2019). Proton Aurora on Mars: A Dayside Phenomenon Pervasive in Southern Summer. *Journal of Geophysical Research: Space Physics*, *124*(12), 10533-10548. Retrieved from https://agupubs.onlinelibrary.wiley.com/doi/abs/10.1029/2019JA027140 doi: https://doi.org/10.1029/2019JA027140

Johnston, B. J., Schneider, N. M., Jain, S. K., Milby, Z., Deighan, J., Bowers, C. F., ... Curry, S. (2023). Discrete Aurora at Mars: Insights Into the Role of Magnetic Reconnection. *Geophysical Research Letters*, *50*(24), e2023GL104198. Retrieved from https://agupubs.onlinelibrary.wiley.com/doi/abs/10.1029/2023GL104198 (e2023GL104198 2023GL104198) doi: https://doi.org/10.1029/2023GL104198

Langlais, B., Thébault, E., Houliez, A., Purucker, M. E., & Lillis, R. J. (2019). A New Model of the Crustal Magnetic Field of Mars Using MGS and MAVEN. *Journal of Geophysical Research: Planets*, *124*(6), 1542-1569. Retrieved from https://agupubs.onlinelibrary.wiley.com/doi/abs/10.1029/2018JE005854 doi: https://doi.org/10.1029/2018JE005854

Leblanc, F., Witasse, O., Lilensten, J., Frahm, R. A., Safaenili, A., Brain, D. A., ... Lundin, R. (2008). Observations of aurorae by SPICAM ultraviolet spectrograph on board Mars Express: Simultaneous ASPERA-3 and MARSIS measurements. *Journal of Geophysical Research: Space Physics*, *113*(A8). Retrieved from https://agupubs.onlinelibrary.wiley.com/doi/abs/10.1029/2008JA013033 doi: https://doi.org/10.1029/2008JA013033

Leblanc, F., Witasse, O., Winningham, J., Brain, D., Lilensten, J., Blelly, P.-L., ... Bertaux, J. L. (2006). Origins of the Martian aurora observed by Spectroscopy for Investigation of Characteristics of the Atmosphere of Mars (SPICAM) on board Mars Express. *Journal of Geophysical Research: Space Physics*, *111*(A9). Retrieved from https://agupubs.onlinelibrary.wiley.com/doi/abs/10.1029/2006JA011763 doi: https://doi.org/10.1029/2006JA011763

Liemohn, M. W., Ma, Y., Frahm, R. A., Fang, X., Kozyra, J. U., Nagy, A. F., ... Lundin, R. (2006, October). Mars Global MHD Predictions of Magnetic Connectivity Between the Dayside Ionosphere and the Magnetospheric Flanks. *Space Science Reviews*, *126*(1-4), 63-76. doi: 10.1007/s11214-006-9116-8

Liemohn, M. W., Ma, Y., Nagy, A. F., Kozyra, J. U., Winningham, J. D., Frahm, R. A., ... Lundin, R. (2007). Numerical modeling of the magnetic topology near Mars auroral

observations. *Geophysical Research Letters*, *34*(24). Retrieved from https://agupubs.onlinelibrary.wiley.com/doi/abs/10.1029/2007GL031806 doi: https://doi.org/10.1029/2007GL031806

Lillis, R. J., & Brain, D. A. (2013). Nightside electron precipitation at Mars: Geographic variability and dependence on solar wind conditions. *Journal of Geophysical Research: Space Physics*, *118*(6), 3546-3556. Retrieved from https://agupubs.onlinelibrary.wiley.com/doi/abs/10.1002/jgra.50171 doi: https://doi.org/10.1002/jgra.50171

Lillis, R. J., Deighan, J., Brain, D., Fillingim, M., Jain, S., Chaffin, M., ... Curry, S. (2022). First Synoptic Images of FUV Discrete Aurora and Discovery of Sinuous Aurora at Mars by EMM EMUS. *Geophysical Research Letters*, *49*(16), e2022GL099820. Retrieved from https://agupubs.onlinelibrary.wiley.com/doi/abs/10.1029/2022GL099820 (e2022GL099820 2022GL099820) doi: https://doi.org/10.1029/2022GL099820

Lundin, R., Winningham, D., Barabash, S., Frahm, R., Brain, D., Nilsson, H., ... Wurz, P. (2006, October). Auroral Plasma Acceleration Above Martian Magnetic Anomalies. *Space Science Reviews*, *126*(1-4), 333-354. doi: 10.1007/s11214-006-9086-x

Lundin, R., Winningham, D., Barabash, S., Frahm, R., Holmström, M., Sauvaud, J. A., ... Wurz, P. (2006, February). Plasma Acceleration Above Martian Magnetic Anomalies. *Science*, *311*(5763), 980-983. doi: 10.1126/science.1122071

Mitchell, D. L., Lin, R. P., Mazelle, C., Rème, H., Cloutier, P. A., Connerney, J. E. P., ... Ness, N. F. (2001). Probing Mars' crustal magnetic field and ionosphere with the MGS Electron Reflectometer. *Journal of Geophysical Research: Planets*, *106*(E10), 23419-23427. Retrieved from https://agupubs.onlinelibrary.wiley.com/doi/abs/10.1029/2000JE001435 doi: https://doi.org/10.1029/2000JE001435

Nakamura, Y., Terada, N., Leblanc, F., Rahmati, A., Nakagawa, H., Sakai, S., ... Murase, K. (2022). Modeling of Diffuse Auroral Emission at Mars: Contribution of MeV Protons. *Journal of Geophysical Research: Space Physics*, *127*(1), e2021JA029914. Retrieved from https://agupubs.onlinelibrary.wiley.com/doi/abs/10.1029/2021JA029914 (e2021JA029914 2021JA029914) doi: https://doi.org/10.1029/2021JA029914

Pacios, D., Vázquez-Poletti, J. L., Dhuri, D. B., Atri, D., Moreno-Vozmediano, R., Lillis, R. J., ... Vázquez, L. (2024). A serverless computing architecture for Martian aurora detection with the Emirates Mars Mission. *Sci Rep*, *14*, 3029. Retrieved from https://doi.org/10.1038/s41598-024-53492-4 doi: 10.1038/s41598-024-53492-4

Phillips, J. L., Stewart, A. I. F., & Luhmann, J. G. (1986). The Venus ultraviolet aurora: Observations at 130.4 nm. *Geophysical Research Letters*, *13*(10), 1047-1050. Retrieved from https://agupubs.onlinelibrary.wiley.com/doi/abs/10.1029/GL013i010p01047 doi: https://doi.org/10.1029/GL013i010p01047

Ritter, B., Gérard, J.-C., Hubert, B., Rodriguez, L., & Montmessin, F. (2018). Observations of the Proton Aurora on Mars With SPICAM on Board Mars Express. *Geophysical Research Letters*, *45*(2), 612-619. Retrieved from https://agupubs.onlinelibrary.wiley.com/doi/abs/10.1002/2017GL076235 doi: https://doi.org/10.1002/2017GL076235

Schneider, N. M., Deighan, J. I., Jain, S. K., Stiepen, A., Stewart, A. I. F., Larson, D., ... Jakosky, B. M. (2015, November). Discovery of diffuse aurora on Mars. *Science*, *350*(6261), 0313. doi: 10.1126/science.aad0313

Schneider, N. M., Jain, S. K., Deighan, J., Nasr, C. R., Brain, D. A., Larson, D., ... Jakosky, B. M. (2018). Global Aurora on Mars During the September 2017 Space Weather Event. *Geophysical Research Letters*, *45*(15), 7391-7398. Retrieved from https://agupubs.onlinelibrary.wiley.com/doi/abs/10.1029/2018GL077772 doi: https://doi.org/10.1029/2018GL077772

Schneider, N. M., Milby, Z., Jain, S. K., Gérard, J.-C., Soret, L., Brain, D. A., ... Jakosky, B. M. (2021). Discrete Aurora on Mars: Insights Into Their Distribution and Activity From MAVEN/IUVS Observations. *Journal of Geophysical Research: Space*

Physics, *126*(10), e2021JA029428. Retrieved from https://agupubs.onlinelibrary.wiley.com/doi/abs/10.1029/2021JA029428 (e2021JA029428 2021JA029428) doi: https://doi.org/10.1029/2021JA029428

Shematovich, V. I., Bisikalo, D. V., Gérard, J. C., & Hubert, B. (2017, September). Changes in the Martian atmosphere induced by auroral electron precipitation. *Solar System Research*, *51*(5), 362-372. doi: 10.1134/S0038094617050094

Soret, L., Gérard, J.-C., Libert, L., Shematovich, V. I., Bisikalo, D. V., Stiepen, A., & Bertaux, J.-L. (2016). SPICAM observations and modeling of Mars aurorae. *Icarus*, *264*, 398-406. Retrieved from https://www.sciencedirect.com/science/article/pii/S0019103515004285 doi: https://doi.org/10.1016/j.icarus.2015.09.023

Soret, L., Gérard, J.-C., Schneider, N., Jain, S., Milby, Z., Ritter, B., ... Weber, T. (2021). Discrete Aurora on Mars: Spectral Properties, Vertical Profiles, and Electron Energies. *Journal of Geophysical Research: Space Physics*, *126*(10), e2021JA029495. Retrieved from https://agupubs.onlinelibrary.wiley.com/doi/abs/10.1029/2021JA029495 (e2021JA029495 2021JA029495) doi: https://doi.org/10.1029/2021JA029495

Steckiewicz, M., Garnier, P., André, N., Mitchell, D. L., Andersson, L., Penou, E., ... Jakosky, B. M. (2017). Comparative study of the Martian suprathermal electron depletions based on Mars Global Surveyor, Mars Express, and Mars Atmosphere and Volatile EvolutioN mission observations. *Journal of Geophysical Research: Space Physics*, *122*(1), 857-873. Retrieved from https://agupubs.onlinelibrary.wiley.com/doi/abs/10.1002/2016JA023205 doi: https://doi.org/10.1002/2016JA023205

Sánchez-Cano, B., Lester, M., Witasse, O., Blelly, P.-L., Indurain, M., Cartacci, M., ... Noschese, R. (2018). Spatial, Seasonal, and Solar Cycle Variations of the Martian Total Electron Content (TEC): Is the TEC a Good Tracer for Atmospheric Cycles? *Journal of Geophysical Research: Planets*, *123*(7), 1746-1759. Retrieved from https://agupubs.onlinelibrary.wiley.com/doi/abs/10.1029/2018JE005626 doi: https://doi.org/10.1029/2018JE005626

Sánchez-Cano, B., Lester, M., Witasse, O., Milan, S. E., Hall, B. E. S., Cartacci, M., ... Pätzold, M. (2016). Solar cycle variations in the ionosphere of Mars as seen by multiple Mars Express data sets. *Journal of Geophysical Research: Space Physics*, *121*(3), 2547-2568. Retrieved from https://agupubs.onlinelibrary.wiley.com/doi/abs/10.1002/2015JA022281 doi: https://doi.org/10.1002/2015JA022281

Uluşen, D., & Linscott, I. (2008). Low-energy electron current in the Martian tail due to reconnection of draped interplanetary magnetic field and crustal magnetic fields. *Journal of Geophysical Research: Planets*, *113*(E6). Retrieved from https://agupubs.onlinelibrary.wiley.com/doi/abs/10.1029/2007JE002916 doi: https://doi.org/10.1029/2007JE002916

Weber, T., Brain, D., Mitchell, D., Xu, S., Connerney, J., & Halekas, J. (2017). Characterization of Low-Altitude Nightside Martian Magnetic Topology Using Electron Pitch Angle Distributions. *Journal of Geophysical Research: Space Physics*, *122*(10), 9777-9789. Retrieved from https://agupubs.onlinelibrary.wiley.com/doi/abs/10.1002/2017JA024491 doi: https://doi.org/10.1002/2017JA024491

Weber, T., Brain, D., Xu, S., Mitchell, D., Espley, J., Halekas, J., ... Jakosky, B. (2020). The Influence of Interplanetary Magnetic Field Direction on Martian Crustal Magnetic Field Topology. *Geophysical Research Letters*, *47*(19), e2020GL087757. Retrieved from https://agupubs.onlinelibrary.wiley.com/doi/abs/10.1029/2020GL087757 (e2020GL087757 10.1029/2020GL087757) doi: https://doi.org/10.1029/2020GL087757

Xu, S., Mitchell, D., Liemohn, M., Dong, C., Bougher, S., Fillingim, M., ... Jakosky, B. (2016). Deep nightside photoelectron observations by MAVEN SWEA: Implications for Martian northern hemispheric magnetic topology and nightside ionosphere source. *Geophysical Research Letters*, *43*(17), 8876-8884. Retrieved from https://agupubs.onlinelibrary.wiley.com/doi/abs/10.1002/2016GL070527 doi: https://doi

.org/10.1002/2016GL070527

Xu, S., Mitchell, D., Liemohn, M., Fang, X., Ma, Y., Luhmann, J., ... Jakosky, B. (2017). Martian low-altitude magnetic topology deduced from MAVEN/SWEA observations. *Journal of Geophysical Research: Space Physics*, *122*(2), 1831-1852. Retrieved from https://agupubs.onlinelibrary.wiley.com/doi/abs/10.1002/2016JA023467 doi: https://doi.org/10.1002/2016JA023467

Xu, S., Mitchell, D. L., McFadden, J. P., Fillingim, M. O., Andersson, L., Brain, D. A., ... Espley, J. (2020). Inverted-V Electron Acceleration Events Concurring With Localized Auroral Observations at Mars by MAVEN. *Geophysical Research Letters*, *47*(9), e2020GL087414. Retrieved from https://agupubs.onlinelibrary.wiley.com/doi/abs/10.1029/2020GL087414 (e2020GL087414 10.1029/2020GL087414) doi: https://doi.org/10.1029/2020GL087414

Xu, S., Mitchell, D. L., McFadden, J. P., Schneider, N. M., Milby, Z., Jain, S., ... Johnston, B. (2022). Empirically Determined Auroral Electron Events at Mars—MAVEN Observations. *Geophysical Research Letters*, *49*(6), e2022GL097757. Retrieved from https://agupubs.onlinelibrary.wiley.com/doi/abs/10.1029/2022GL097757 (e2022GL097757 2022GL097757) doi: https://doi.org/10.1029/2022GL097757

Xu, S., Weber, T., Mitchell, D. L., Brain, D. A., Mazelle, C., DiBraccio, G. A., & Espley, J. (2019). A Technique to Infer Magnetic Topology at Mars and Its Application to the Terminator Region. *Journal of Geophysical Research: Space Physics*, *124*(3), 1823-1842. Retrieved from https://agupubs.onlinelibrary.wiley.com/doi/abs/10.1029/2018JA026366 doi: https://doi.org/10.1029/2018JA026366